2.07 Mineralogy of Super-Earth Planets

T Duffy, Princeton University, Princeton, NJ, USA
N Madhusudhan, University of Cambridge, Cambridge, UK
KKM Lee, Yale University, New Haven, CT, USA

2.07.1 Introduction

The past two decades in modern astronomy have seen astounding success in discovering planets orbiting stars beyond the solar system. Starting with the first detections of planets orbiting neutron stars (Wolszczan and Frail, 1992) and those orbiting sunlike stars (Marcy and Butler, 1996; Mayor and Queloz, 1995), over 900 confirmed extrasolar planets or 'exoplanets' are now known. These planets have been discovered by a variety of techniques. By far, the largest number has been identified by the radial velocity method, which involves observing the wobbling of the host star due to the gravitational pull by the planet along the line of sight of the observer. The amplitude of the radial velocity of the stellar motion places a lower limit on the planetary mass, while the period gives the orbital period of the planet. Another major approach to exoplanet detection has been the transit method, whereby the passage of the planet in front of the host star is seen in the temporary dimming of the stellar light as observed from Earth. The transit method ushered in a major advance in the characterization of exoplanets as it allows the measurement of the planetary radius and the orbital inclination of the system, which conclusively determines the planetary mass when radial velocity observations are available. One of the greatest successes in discovering exoplanets have been achieved by the Kepler space telescope (Batalha et al., 2013; Borucki et al., 2010), which has discovered (as of July 2013) 134 confirmed exoplanets and over 3200 exoplanet candidates with a wide range of exoplanetary properties. Exoplanets have also been detected by other methods such as pulsar timing (Wolszczan and Frail, 1992), gravitational microlensing (Gaudi et al., 2008), and direct imaging (Kalas et al., 2008), covering different regions of exoplanet parameter space. For further details, see **Chapter 10.21**.

The numerous exoplanet discoveries via different methods have also led to the estimation of occurrence rates of exoplanets over a wide range of planetary masses and radii, ranging from gas giant planets to sub-Neptune and even terrestrial-size planets in the solar neighborhood (Fressin et al., 2013; Howard et al., 2012). The available statistics indicate a planetary mass (size) function increasing with decreasing planet mass (size), namely, that giant planets are comparatively rare (Howard et al., 2012; **Figure 1**). It is estimated that 15% of sunlike stars host at least one planet of 3–30 Earth masses (M_E), and an additional 14% of such stars have planets with 1–3 M_E (Howard, 2013). Correlations of the planet occurrences with the metallicities of the host stars have also suggested that formation of giant planets is positively correlated with the metallicities of the stellar hosts (Fischer and Valenti, 2005), whereas low-mass planets are uncorrelated with the stellar metallicity (Buchhave et al., 2012). Besides the statistical correlations, exoplanets detected to date span a wide diversity in orbital parameters (orbital periods, separations, eccentricities, inclinations, etc.), masses, radii, and temperatures, much wider than the phase space spanned by planets in our solar system. In recent years, it has even become possible to observe the atmospheres of a wide range of exoplanets (e.g., Seager and Deming, 2010).

The latest exoplanet surveys are increasingly focusing on discovering low-mass planets around nearby stars, with the ultimate aim of discovering Earth analogs in nearby stellar systems. To date, masses and radii have already been measured for over a dozen super-Earths, defined as those planets with masses between 1 and 10 M_E (see the succeeding text). Understanding the interiors and atmospheres of these super-Earths represents a new frontier in exoplanet science. There are no super-Earth analogs in our solar system. Limited data available at present suggest that super-Earths may span a wide range of possible compositions from iron-rich super-Mercuries and molten lava planets to water worlds with thick steamy envelopes and planets dominated by carbon. It is not yet known what fraction of super-Earths are scaled-up versions of terrestrial planets and which are scaled-down versions of ice giants such as Neptune or lie somewhere in the continuum between these compositions.

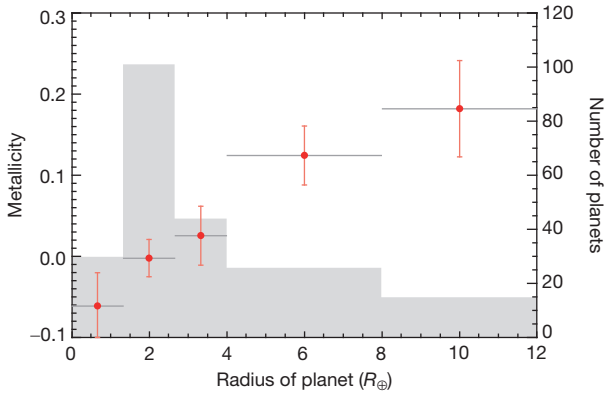

Figure 1 Average metallicity (proportion of elements heavier than H and He) for planet-hosting stars and a number of observed planets plotted as a function of planetary radius. The red symbols show the average metallicity of the host stars with planets of different radii grouped in 1.33 Earth radii and 4 Earth radii bins. The bin size is indicated by the length of the horizontal line, and the uncertainty in the average metallicity is given by the standard deviation. The gray histogram gives the number of planets in each bin. Reproduced from Buchhave et al. (2012) An abundance of small exoplanets around stars with a wide range of metallicities. *Nature* 486: 375–377, with permission.

Knowledge of the mineralogy of super-Earth planets is essential to understanding their interior structure, thermal behavior, and long-term evolution. The mineralogy will depend on bulk composition and the pressures and temperatures of the interior. The large sizes of super-Earth planets mean that interior pressures are very high, posing a severe challenge for laboratory experiments attempting to reproduce super-Earth conditions. Quantum mechanical theoretical methods offer an effective alternative means to evaluate interior mineralogy, but such methods require testing and confirmation by experiment. New laboratory techniques for extending the accessible pressure range are undergoing rapid development. Combined with the fast pace of advances in astronomical detection, observation, and modeling of extrasolar planets, it is clear that the study of super-Earth planets, while in its infancy today, will expand rapidly in the coming years. This chapter reviews our current understanding of mineral behavior at extreme pressure (P)–temperature (T) conditions and its possible implications for super-Earth planets. It is expected that future developments will likely require substantial revisions in this understanding, but much progress has been made to date, and a summary of this progress is undertaken here. Other recent review articles discussing possible internal structures and mineralogy of exoplanets can be found elsewhere (Sotin et al., 2010; Valencia, 2013).

2.07.2 Overview of Super-Earths

2.07.2.1 What Is a Super-Earth?

The term 'super-Earth' refers canonically to planets with masses between 1 and 10 M_E (Seager et al., 2007; Valencia et al., 2006). The upper limit of 10 M_E, though not well defined, is motivated by the mass limit beyond which a solid protoplanetary core is expected to be able to gravitationally attract and retain H_2–He gas from the surrounding nebula and thereby grow into a Neptune- or Jupiter-sized planet. The corresponding radii of super-Earths are generally in the range of 1–2.5 Earth radii, though a few members above 2.5 Earth radii are now known. As discussed elsewhere in this chapter, super-Earths can plausibly encompass a wide range of compositions, but here, we will focus our attention primarily on terrestrial-type compositions, although possible planets enriched in carbon and water will also be discussed.

We expect that the super-Earth family will encompass a broad range of physical properties and orbital characteristics and thus have the potential to exhibit a wide variety of climactic regimes ranging from very hot for planets close to their stars to beyond the ice line for planets at a great distance from their hosts. The question of habitability of super-Earths is obviously one of central importance (Seager, 2013). While this topic is not directly addressed here, the interior mineralogy will influence key habitability factors including the nature and

composition of the atmosphere, existence of plate tectonics, and capacity to generate an internal magnetic field.

With no analogs in the solar system, it is presently unclear what fraction of super-Earths are scaled-up terrestrial planets and what fraction are scaled-down giant planets, which might have lost their primordial envelopes to atmospheric escape. The atmospheres of super-Earths may resemble those of ice giants such as Uranus and Neptune with thick hydrogen-rich atmospheres or terrestrial planets with secondary atmospheres composed of heavy molecules such as CO_2, O_2, H_2O, or other components. Other possibilities having no solar system analog include water-dominated atmospheres in planets that formed beyond the snow line and migrated inward or planets with secondary atmospheres of outgassed H_2 (which might affect the radius of the planet even for small amounts of hydrogen) (Rogers and Seager, 2010). Detailed observations and characterization of super-Earths are one of the most dynamic areas of exoplanetary science today, with several unsolved problems at the intersections of astrophysics, planetary science, and geoscience.

2.07.2.2 Observations of Super-Earths

The past few years have seen a rise in the discoveries of super-Earths. Increased photometric precision in transit surveys now allows detection of planets even below Earth's size. However, since transit surveys can only measure the size but not the mass, independent constraints on the planet masses need to be obtained from alternative methods. Using the radial velocity method, currently achievable Doppler precisions have allowed measurement of exoplanet masses down to $\sim 5\ M_E$ for super-Earths in close orbits around stars of varied spectral types (Charbonneau et al., 2009; Léger et al., 2009; Winn et al., 2011). An alternative approach to measure mass has been made possible by detections of multiplanet systems by the Kepler space telescope. By measuring the transit timing variations of a transiting exoplanet induced by gravitational interactions with other planets in the system, the mass of the transiting exoplanet can be inferred dynamically. This approach has led to mass measurements of many of the transiting super-Earths known to date. Figure 2 shows the super-Earths for which masses and radii have been measured so far. The Kepler space telescope has discovered all but four of these super-Earths, and the masses of many of them have been determined dynamically. Measuring masses of all these Kepler planets would not have been possible using the radial velocity method alone because their host stars are too faint for the required radial velocity precision. For the same reason, observing the atmospheres of these Kepler planets is very difficult with current observational capabilities.

One of the major thrusts in exoplanet research is to detect super-Earths orbiting low-mass stars and nearby bright stars. The advantage of finding low-mass stars hosting super-Earths is that for a given super-Earth mass and orbital period, the measurement of both the planet mass and the planet radius becomes easier for lower stellar mass and radius – that is, both the radial velocity and the transit signals are larger. On the other hand, brighter stars allow greater precision in the mass and radius measurements. Both these situations are also particularly favorable to observe super-Earth atmospheres, since the favorable

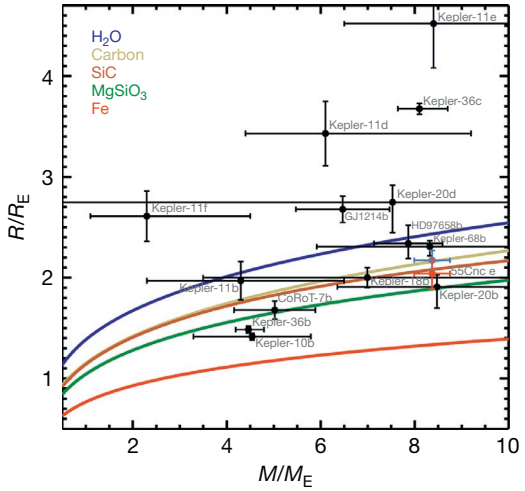

Figure 2 Mass–radius relations of super-Earths. The colored curves show mass–radius relations predicted by internal structure models of solid planets of uniform composition composed of the different species indicated in the legend. The black symbols with error bars show measured radii and masses of known transiting super-Earths. Two possible values of radii are shown for 55 Cancri e (55 Cnce). The red data point shows the radius measured in the visible, and the blue data point shows a gray radius obtained by combining visible and infrared measurements. For Corot-7b, there are multiple measurements of the mass as discussed in the text. Only the lower mass determination is shown here. Planetary properties were obtained from the Exoplanet Orbit Database (Wright et al., 2011) and the Exoplanet Data Explorer at exoplanets.org. Modified from Madhusudhan N, Lee KKM, and Mousis O (2012) A possible carbon-rich interior in super-Earth 55 Cancri e. *Astrophysical Journal Letters* 759(2): L40. http://dx.doi.org/10.1088/2041-8205/759/2/L40, with permission.

stellar parameters allow better precision for spectroscopic observations of the super-Earths in the infrared. Consequently, of all the super-Earths known to date, two are known to be particularly good candidates for detailed characterization of their interiors and atmospheres: (1) GJ 1214b, a super-Earth orbiting a low-mass M Dwarf star, and (2) 55 Cancri e, a super-Earth orbiting a nearby bright sunlike star. These and other super-Earths are discussed in more detail in the succeeding text.

2.07.2.3 Interior Structure and Mass–Radius Relationships

Interior structure models for exoplanets are essential for interpreting observations of their masses, radii, and atmospheres and for understanding the physicochemical diversity of planetary systems. Detailed interior models exist for Earth and other solar system planets satisfying geophysical observables and geochemical and cosmochemical constraints (see Chapter 10.02). Models for exoplanets are constructed in a similar way by assuming a spherically symmetric planet in hydrostatic equilibrium. The planet is taken to be fully differentiated and sorted into layers of increasing density with a fixed composition in each layer. The interior structure is obtained by solving a set of coupled differential equations for mass $m(r)$, pressure $P(r)$, and density $\rho(r)$, using the equations for hydrostatic equilibrium:

$$\frac{dP(r)}{dr} = -\frac{Gm(r)\rho(r)}{r^2} \quad [1]$$

the mass of a spherical shell

$$\frac{dm(r)}{dr} = 4\pi r^2 \rho(r) \quad [2]$$

and an equation of state (EOS)

$$\rho(r) = f(T(r), P(r)) \quad [3]$$

where r is the radial distance from the planet's center, G is the gravitational constant, and T is the temperature.

Depending on composition, the interior models may include layers representing an outer atmosphere or ocean, ice layer, silicate mantle, and metallic core. Some layers may be further subdivided due to phase or chemical changes within a given region. The first detailed interior models for massive terrestrial planets were constructed by Valencia et al. (2006). Subsequently, a number of additional models have been reported (Fortney et al., 2007; Gong and Zhou, 2012; Grasset et al., 2009; Madhusudhan et al., 2012; Rogers and Seager, 2010; Seager et al., 2007; Sotin et al., 2007; Swift et al., 2012; Wagner et al., 2012). In addition to terrestrial-type super-Earths, models have also explored, for example, Fe-rich (super-Mercuries) (Valencia et al., 2006), H_2O-rich ('ocean' planets) (Sotin et al., 2007), and C-rich compositions ('diamond' planets) (Madhusudhan et al., 2012).

The temperature distribution in the interior depends on a number of factors such as the initial temperature resulting from accretion processes, the distribution of heat sources in the interior, and the rate of heat transport, as well as the external boundary condition set by incident irradiation from the host star and any insulating effects of an overlying atmosphere. While the temperature gradient throughout much of the interior is likely to be adiabatic, the actual temperature is only loosely constrained due to the uncertainties mentioned earlier. Some interior models to date have incorporated detailed thermal models by making various assumptions about physicochemical conditions and thermal properties in the planet, whereas other models have mainly ignored thermal effects or treated them in a simplified manner so far.

Surface temperatures of known super-Earths are expected to range from ~600 to ~2500 K (Figure 3), which is a reflection of the close orbital distances of most detections so far. The upper range of surface temperatures is above the melting temperatures of silicates and thus may result in the formation of a magma ocean and a thick atmosphere due to extensive degassing from the planet's interior. Cooler surface temperatures allow for a brittle crust and potentially volatile-rich oceans and atmospheres.

The interior model constrains mass–radius scaling relationships that allow for interpretation of observational data on exoplanets in terms of composition. For terrestrial compositions, Valencia et al. (2006) obtained the following mass (M)–radius (R) scaling expression for planets with 1–10 M_E:

$$\frac{R}{R_E} = \left(\frac{M}{M_E}\right)^{0.267-0.272} \quad [4]$$

where R_E and M_E are the radius and mass of the Earth. Other studies have reported similar relationships (Grasset et al., 2009; Sotin et al., 2007). For a representative ocean planet containing

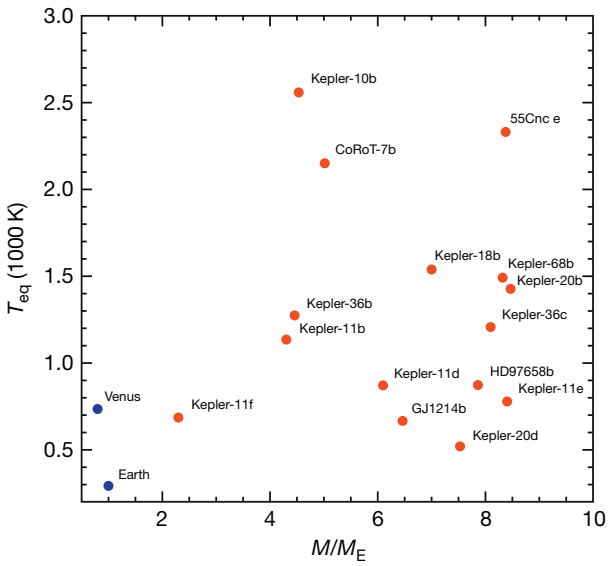

Figure 3 Planetary equilibrium temperature versus mass for super-Earths detected to date. Planetary properties were obtained from the Exoplanet Orbit Database (Wright et al., 2011) and the Exoplanet Data Explorer at exoplanets.org.

50 wt% H_2O and 50 wt% refractory material (rock and metal), the corresponding expression is (Sotin et al., 2007)

$$\frac{R}{R_E} = 1.262\left(\frac{M}{M_E}\right)^{0.275} \quad [5]$$

The interior models are used to make inferences regarding internal structure and dynamics, cooling histories, magnetic field generation, and other planetary properties. Figure 2 illustrates how the observed mass–radii values for super-Earths compare with predictions from internal structure models for solid planets with selected uniform compositions. These end-member models delineate the ranges of masses and radii that can exist for different categories of planets. In a more detailed approach, Wagner et al. (2012) constructed a four-layer structural model for rocky exoplanets by combining eqns [1]–[3] with energy balance equations and used these to model the structure and internal dynamics of two recently discovered super-Earths. Figure 4 shows the range of interior P–T conditions predicted from their model for selected planetary masses. Other studies produce broadly similar results for terrestrial-type compositions (e.g., Sotin et al., 2007; Valencia et al., 2006). The core–mantle boundary and central pressure as a function of planetary mass are shown in Figure 5, for both the rocky exoplanet modeled by Wagner et al. (2012) and an ocean planet consisting of 50% rocky material of terrestrial composition and 50% H_2O (Sotin et al., 2007). Compared to Earth where the core–mantle boundary pressure is 135 GPa and ~3000–4000 K, the conditions in a 10 M_E terrestrial or ocean planet reach ~1200 GPa and ~6000–7000 K. The corresponding central pressure ranges from ~2400 GPa and ~6500 K (ocean planet) to 3900 GPa and ~10 000 K (terrestrial planet) (compared with 363 GPa and ~6000 K for Earth).

Interpretation of observed mass–radius data for exoplanets in terms of compositional models is limited by observational uncertainties, model assumptions, and inherent degeneracies

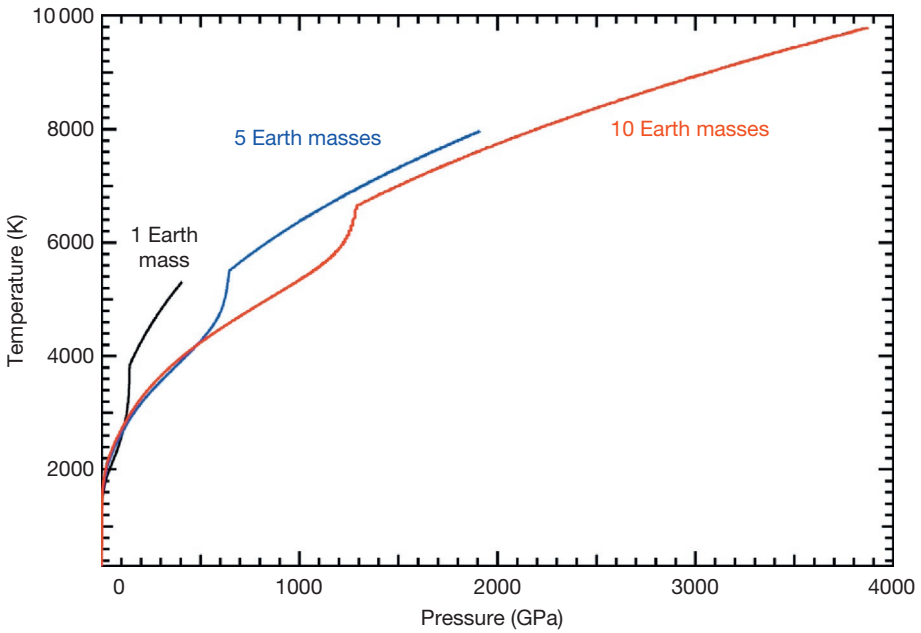

Figure 4 Internal pressures and temperatures from an internal structure model for Earth-like planets for the range of masses indicated. Reproduced from Wagner FW, Tosi N, Sohl F, Rauer H, and Spohn T (2012) Rocky super-Earth interiors. *Astronomy and Astrophysics* 541: A103. http://dx.doi.org/10.1051/0004-6361/201118441, with permission.

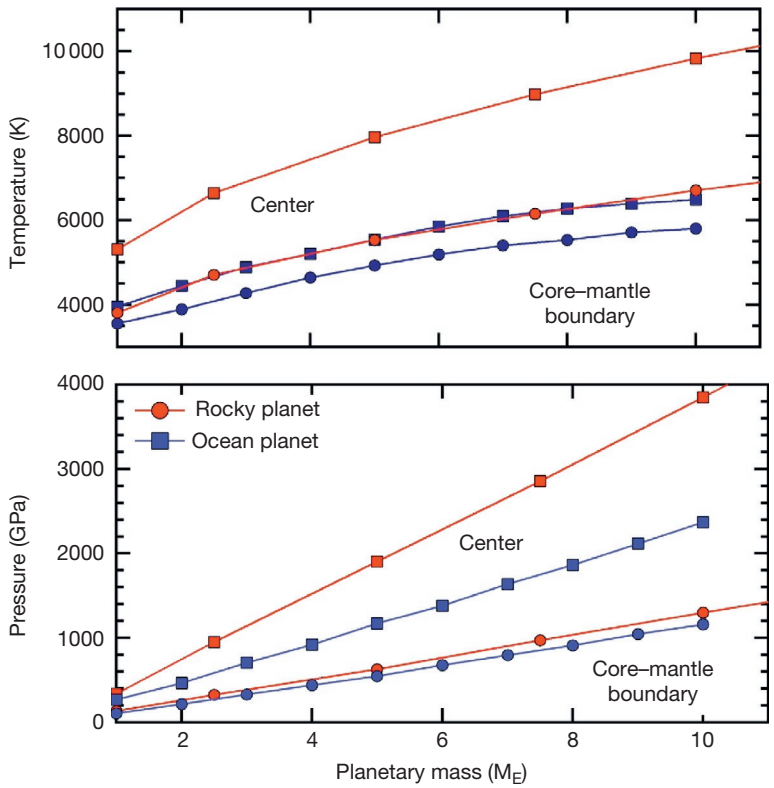

Figure 5 Temperature and pressure at the core–mantle boundary and center of super-Earths as a function of mass for an Earth-like composition (Wagner et al., 2012) and ocean planet containing 50% H_2O (Sotin et al., 2007).

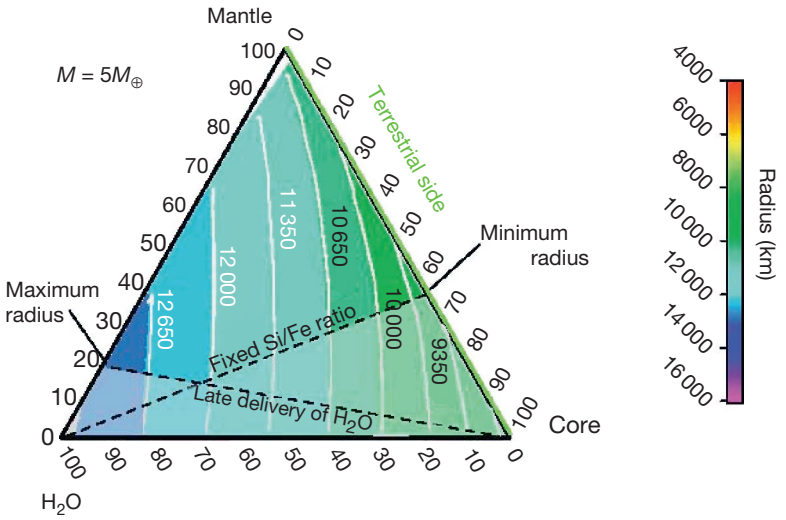

Figure 6 Ternary diagram showing range of possible compositions for a 5 M_E planet with components of H_2O, mantle (silicate), and core (iron). Each point inside the diagram uniquely specifies a composition and corresponding radius. The smallest radius corresponds to a pure iron planet and the largest radius corresponds to a pure H_2O planet. Reproduced from Valencia D, O'Connell RJ, and Sasselov DD (2009) The role of high-pressure experiments on determining super-Earth properties. *Astrophysics and Space Science* 322(1–4): 135–139. http://dx.doi.org/10.1007/s10509-009-0034-6, with permission.

(Rogers and Seager, 2010). There are a variety of sources of observational uncertainties. Planet mass, radius, and equilibrium temperature are measured relative to the host star, so reducing uncertainties in host star properties and improved measurement precision can better constrain planetary properties. Beyond this, there remains a fundamental limitation in the ability to determine composition given the limited constraint of mean density. In many cases, a wide span of compositions can fit the available data (Rogers and Seager, 2010; Valencia et al., 2006). **Figure 6** illustrates the compositional degeneracies in a 5 M_E planet consisting of H_2O, a silicate mantle, and an iron core (Valencia et al., 2009). Additional constraints, such as atmospheric composition, may allow one to distinguish among possible compositions. Uncertainties in model assumptions such as the pressure–temperature–density relation are also important and are discussed further in the succeeding text.

2.07.2.4 Selected Super-Earths

To show the richness in potential super-Earth mineralogy, here, we summarize the characteristics and possible internal compositions of a few selected super-Earths.

CoRoT-7b was the first super-Earth planet to have its radius determined (Léger et al., 2009). The value of this property from transit observations is 1.58 (0.10) R_E (Bruntt et al., 2010). The mass is uncertain due to the high activity level of the host star, and recent measurements yield $M_P = 5.2 \pm 0.8$ M_E (Bruntt et al., 2010) or $M_P = 7.42 \pm 1.21$ M_E (Hatzes et al., 2011) with nonoverlapping uncertainties. These correspond to average densities of 7.2 ± 1.8 and 10.4 ± 1.8 g cm^{-3}, respectively. For comparison, the mean density of Earth is 5.5 g cm^{-3}. The densities indicate that the planet has a dominantly rock–metal interior structure (**Figure 2**). Models to date yield compositions ranging from an Earth-like composition with a core of ~30% of the mass for the lower-density case to a more Mercury-like composition with a core that is 2/3 of the total mass for the high-density case (Wagner et al., 2012). In detail, models predict that the density of the mantle increases by a factor of ~2.2–2.5 from the surface value to the core–mantle boundary (Wagner et al., 2012). The central pressure is estimated to be as high as 2000 GPa in the low-density case and 4000 GPa for the high-density model (Swift et al., 2012; Wagner et al., 2012). The density of the Fe core at the center of the planet is estimated to be ~22 g cm^{-3} (Léger et al., 2011; Wagner et al., 2012), representing approximately a threefold compression of iron compared with ambient conditions.

CoRot-7b orbits very closely to its host star (G type) with a semimajor axis of ~0.017 AU. Thus, the surface is expected to be very hot, and as the planet is tidally locked, a large variation in dayside (~2500 K) and nightside (50–75 K) temperatures is expected (Léger et al., 2011). This may result in the formation of a lava ocean on the stellar-facing hemisphere of the planet (Léger et al., 2011). Questions surrounding the origin of CoRot-7b have also attracted interest. It has been speculated that this planet could be a chthonian planet, resulting from the stripping away of a gas or ice giant's outer layers due to proximity to its host star and leaving behind only the residual central core (Lecavelier des Etangs et al., 2004). However, recent mass-loss models suggest that Corot-7b was most likely always a rocky planet (Leitzinger et al., 2011).

Another recently detected planet with similar properties is Kepler-10b. Its radius (~1.4 R_E) and mass (~4.6 M_E) yield a high average density (~8.8 g cm^{-3}) (Batalha et al., 2011). It also orbits a G-type parent star at a close distance ($a = 0.0168$ AU). The interior composition is predicted to be Mercury-like, similar to the high-density case for CoRoT-7b (Wagner et al., 2012).

GJ 1214b appears to be intermediate between terrestrial planets such as the Earth and the ice giants Neptune and

Uranus. It has a mass of $6.55 \pm 0.098\ M_E$, but its density (1.87 ± 0.40 g cm^{-3}) is only ~1/3 that of the Earth. Possible interior models include a rocky planet with an outgassed atmosphere, a scaled-down version of Neptune (i.e., sub-Neptune, a rocky/icy core with hydrogen-rich atmosphere), or an ice-dominated interior analogous to Jupiter's icy satellites (Rogers and Seager, 2010). In any case, the low density implies that it almost certainly has a significant gas component. A discussion of current understanding of this planet's atmosphere is contained in the succeeding section.

55 Cancri e is a super-Earth orbiting a nearby G8V star with an orbital period of 18 h. It has a mass of $8.37 \pm 0.38\ M_E$ and a radius of $2.04 \pm 0.15\ R_E$ (Endl et al., 2012; Gillon et al., 2012) yielding a density of ~5.43 g cm^{-3}, similar to the mean density of the Earth. The interior composition has been suggested to be composed of refractory materials (silicates and iron) with an envelope (>10% by mass) of supercritical water (Demory et al., 2011; Gillon et al., 2012; Winn et al., 2011). As an alternative, the interior may be composed of Fe, C, SiC, and/or silicates without a volatile envelope (Madhusudhan et al., 2012). **Figure 7** shows the range of silicate, metals, carbide, and carbon compositions that can satisfy observational data for this planet. Such a carbon-rich composition is plausible if the protoplanetary disk reflected the composition of the host star, which has been reported to be carbon-rich (Delgado Mena et al., 2010). The possibility of carbon-rich planets with interiors dominated by Fe, C, SiC, and/or silicates has previously suggested based on stellar compositional abundances and planetary formation models (Bond et al., 2010; Kuchner and Seager, 2005; Madhusudhan et al., 2011). Planets with carbon-rich interiors represent a potential new regime of interior structure, composition, and evolution compared to planets within our solar system.

2.07.2.5 Super-Earth Atmospheres

Only recently it has become possible to observe the atmospheres of super-Earths. As discussed in Section 2.07.2.2, observing super-Earth atmospheres requires particularly favorable conditions in terms of the stellar hosts, that is, the star has to be either relatively small or particularly bright. Atmospheric observations have been reported for only two super-Earths to date, GJ 1214b (Bean et al., 2010) and 55 Cancri e (Demory et al., 2011, 2012), of which GJ 1214b is by far the most studied. Transmission spectra of the atmosphere of GJ 1214b have not revealed any molecular features over a wide wavelength range (0.6–5 μm). The observed spectra are consistent with either an atmosphere with a high mean molecular weight, implying a small scale height and hence nondetection of molecular features within the precision of the data, or the presence of thick clouds in the atmosphere, which may be hydrogen-rich, thereby masking any molecular features. Limited photometric data are also available for the super-Earth 55 Cancri e, which suggest multiple possible atmospheric compositions, depending on what is assumed for the interior composition. If an Earth-like oxygen-rich interior is assumed, the planet is expected to host a thick envelope of supercritical water of 20% by mass of the planet (Gillon et al., 2012; Winn et al., 2011). However, Madhusudhan et al. (2012) suggested that the planet could be carbon-rich in its interior, in which case available infrared data can be explained by a variety of different atmospheric scenarios, including no atmosphere at all.

As the study of super-Earth atmospheres is still in its infancy, several questions of observational and theoretical significance lay open at the forefront. As alluded to earlier, one of the key questions at the heart of the field concerns distinguishing which super-Earths are Neptune-like and which are Earth-like or have other compositions. Chemical characterization of

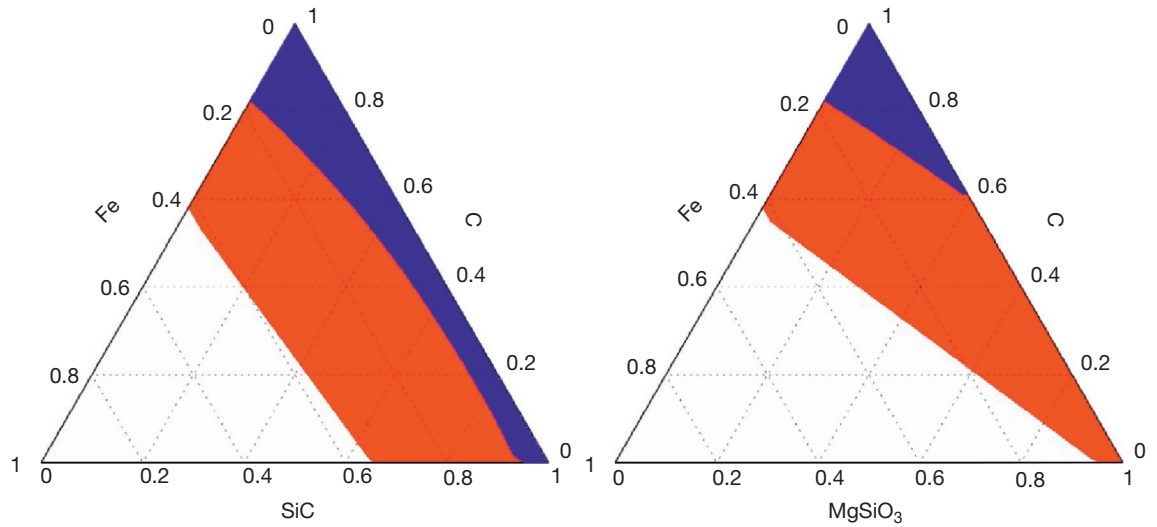

Figure 7 Ternary diagrams showing the range of interior compositions allowed by the mass and radii of 55 Cancri e. Two classes of interior models were considered based on planetesimal compositions predicted by the stellar abundances. (Left) Models composed of Fe, SiC, and C. (Right) Models composed of Fe, $MgSiO_3$, and C. In each case, the red and blue contours show the constraints from the two reported values of measured radius for this planet (see **Figure 2**). The blue contours are subsets of the red contours. The three axes in each case show the mass fractions of the corresponding species. Reproduced from Madhusudhan N, Lee KKM, and Mousis O (2012) A possible carbon-rich interior in super-Earth 55 Cancri e. *Astrophysical Journal Letters* 759(2): L40. http://dx.doi.org/10.1088/2041-8205/759/2/L40, with permission.

their atmospheres may be a key step for distinguishing among degenerate compositional models. On the other hand, currently known super-Earths span an extremely wide range in thermochemical surface conditions (Figure 3). As such, the possible atmospheric chemical compositions of super-Earths are also diverse, beyond the gross distinction of H_2-rich versus H_2-poor. While super-Earth atmospheres at the cooler end can host vast complexes of condensates and aerosols (Miller-Ricci and Fortney, 2010; Morley et al., 2013), the hottest of super-Earths can host atmospheres of vaporized refractory species, such as silicate-rich atmospheres (e.g., Schaefer et al., 2012). The extent and nature of volatile content in super-Earth atmospheres is also intricately linked to their evolutionary history. Depending on their original mass, age, stellar properties, and paths of formation and migration, some super-Earths may retain significant envelopes of volatile species such as H_2 or water vapor for a significant fraction of their lives, whereas others would be expected to have lost most of their original atmospheres (e.g., Lopez et al., 2012). Most importantly, the atmospheric compositions of super-Earths are intricately linked to their interior compositions. Traditionally, atmospheres of super-Earths have largely been studied assuming water as the key volatile (Lopez et al., 2012; Rogers and Seager, 2010; Valencia et al., 2007a), motivated by the oxygen-rich composition of the Earth. However, alternate interior compositions may lead to very different atmospheric compositions. For example, carbon-rich super-Earths (e.g., Madhusudhan et al., 2012) may be devoid of significant amounts of water vapor in the atmosphere, as water ice may be chemically inhibited in carbon-rich formation environments. Consequently, understanding the atmospheres and interior mineralogies of super-Earths is a critical step in assessing the phase space of possible compositions for these bodies.

2.07.3 Theoretical and Experimental Techniques for Ultrahigh-Pressure Research

Interpretation of mass–radius relationships for super-Earths requires knowledge of the equation of state (EOS) of planetary materials, and construction of detailed thermal and evolutionary models requires further understanding of a broader range of thermodynamic, rheological, and transport properties. The P–T conditions of super-Earth interiors (Figures 4 and 5) typically lie above the range of direct laboratory experiments but below the validity of ultrahigh-pressure theoretical EOSs such as the Thomas–Fermi–Dirac (TFD) model (Valencia et al., 2009). This section summarizes the basic theoretical and experimental approaches now being used to explore and predict the relevant material properties under super-Earth conditions.

2.07.3.1 Theoretical Methods

Planetary materials are now routinely studied by means of first-principles or ab initio quantum mechanical simulations. These methods refer to calculations based on the many-body Schrödinger equation, where empirically determined parameters are not used; thus, these methods are based solely on the properties of electrons and nuclei with no input from experiment. Although approximations to these methods are necessary in order to efficiently solve the equations, these approximations are well tested for a wide range of materials and conditions.

Density functional theory (DFT) is arguably the most successful first-principles method to study the high-pressure (ground-state) behavior of terrestrial materials and has been described in detail elsewhere (e.g., Gillan et al., 2006; Wentzcovitch and Stixrude, 2010; **Chapters 2.08** and **2.11**). Approximations such as the local density approximation (LDA) and generalized gradient approximation (GGA) are used in practice with DFT to treat the exchange and correlation between the electrons in the computation of energies. To include high-temperature effects requires more demanding computations than for ground-state (i.e., zero-temperature) simulations because at high temperature, the free energy plays the essential role, and an accurate calculation of this requires expensive sampling of phase space.

DFT calculations have been extensively tested against experiment at lower pressures, and the successes and limitations of the method are well established. For many planetary materials, the accuracy of LDA and GGA is typically ~1–2% for bond lengths and unit cell dimensions, ~5% for vibrational frequencies, and ~15% for elastic constants (Oganov et al., 2013). At the extreme conditions of exoplanets and giant planet cores, DFT methods are not well tested as yet. Current implementations of DFT use pseudopotentials, which are effective potentials that describe the valence electrons but exclude core electrons. Pseudopotential calculations may not be accurate when compressions are sufficiently high such that core electrons begin to participate in chemical bonds (Umemoto et al., 2006a). In such cases, the use of all-electron methods or pseudopotentials that include core orbitals would be necessary. One study that compared Fe pseudopotentials to all-electron calculations at super-Earth pressures yielded identical results with the two methods, supporting the continued reliability of pseudopotential methods (Cottenier et al., 2011).

For materials at moderate temperatures (i.e., less than the Debye temperature), a generally useful approach is the quasiharmonic approximation (QHA), where the potential energy of the crystal is expanded to second order in the displacement of the atoms from their equilibrium positions. This has been shown to work well for important Earth minerals such as ferropericlase (Mg,Fe)O and Mg-silicate perovskite (Mg,Fe,Al)SiO_3, although there are exceptions such as Ca-silicate perovskite, $CaSiO_3$, due to its anharmonicity (Wentzcovitch et al., 2010). The QHA method has been applied to determine phase diagrams of $MgSiO_3$, SiO_2, $CaSiO_3$, etc. (Tsuchiya and Tsuchiya, 2011; Umemoto and Wentzcovitch, 2011; Wu et al., 2011), under super-Earth interior conditions as discussed in the succeeding text, but it has not yet been well tested through comparison with experiment at ultrahigh pressures.

For highly anharmonic solids and liquids or harmonic solids at higher temperatures, molecular dynamics (MD) or Monte Carlo (MC) techniques are used to sample phase space. For MD, the approach is to move the ions according to the Newton's equations of motion (e.g., $F_i = m_i dv_i/dt$) where each atom i has a mass m, velocity v, and force F acting upon it. With appropriately small time steps (e.g., <1/20th of a

vibrational period), one can approximate the solution of the equation of motion (Verlet, 1967). MD simulations are attractive because they also provide information on dynamics and can be used to simulate diffusion behavior, viscosities, and electrical and transport properties, all of which are important for understanding the interiors and evolution of exoplanets (Swift et al., 2012). MC techniques, such as path integral MC, are among the most accurate finite-temperature quantum simulation methods available as they include all correlation effects and track all electrons and the nuclei (Ceperley, 2010). They are efficient at high temperatures (>∼5000 K) and can provide a good description of matter reaching up to a fully ionized plasma state. At lower temperatures, the computations become prohibitively expensive, and thus, it becomes more efficient to use a ground-state simulation method such as quantum MC (Ceperley, 2010).

For the mineralogy expected for super-Earths, these high-temperature methods have not been widely employed yet at super-Earth conditions (e.g., Seager et al., 2007) especially as compared to models for the interiors of Jupiter (or larger)-sized planets where the most abundant elements, H and He, are very sensitive to temperatures (e.g., Militzer and Hubbard, 2009). For heavier materials, the effect of temperature is less important for the EOSs and the resulting mass–radius relationships that are computed from them. High-temperature studies, however, are important for determining the thermal state of a planet and its thermochemical and thermomechanical evolution.

An important recent stride in first-principles theory is the development of approaches for crystal structure prediction that do not require candidate structures as input. This can be particularly useful under the extreme pressures of exoplanets where information on possible crystal structures may be uncertain or incomplete. Ab initio crystal structure prediction requires methods to search through the potentially large space of possible structures to locate the ground-state structure in an efficient manner. Approaches developed for this include evolutionary algorithms (Glass et al., 2006) and random structure searching (Pickard and Needs, 2011). Applications of these methods so far at exoplanet-relevant pressures include studies of carbon (Martinez-Canales et al., 2012), iron (Pickard and Needs, 2009), and the Mg–O system (Zhu et al., 2013). It is expected that many more applications of these approaches will be forthcoming in the future.

2.07.3.2 Experimental Techniques

High-pressure experimental techniques can be divided into static and dynamic methods. For achieving high static pressures, the diamond anvil cell (DAC) provides the widest pressure–temperature coverage. Dynamic experiments fall into two categories: shock compression and ramp compression. Shock compression techniques are well established and have been applied to many types of materials. Ramp compression is an emerging technique with the potential to cover regions of P–T space not easily accessed with either DACs or conventional shock methods. Each of these techniques is discussed in turn in this section.

2.07.3.2.1 Diamond anvil cell

The DAC is the most widely used device for high-pressure research (see **Chapter 2.11**). In DAC experiments, a small (∼10–100 μm) sample is compressed between two gem-quality diamonds. The highest reported pressure achieved in the DAC to date is 640 GPa (Dubrovinsky et al., 2012), but the vast majority of DAC measurements are carried out at less than 200 GPa. The sample can be heated while under pressure using resistive or laser heating techniques allowing temperatures up to several thousand Kelvin to be achieved. Recently, the highest combined P–T conditions yet achieved in the laser-heated DAC, approaching 400 GPa and 6000 K, have been reported (Tateno et al., 2010).

The transparency of diamond in the visible, infrared, and x-ray portions of the spectrum enables application of a variety of optical and x-ray techniques under *in situ* high-pressure conditions with this device. Static compression studies using the DAC have thus enabled exploration of a wide range of phenomena in materials at pressures of up to ∼200 GPa and temperatures ranging from near zero to several thousand Kelvin. The study of crystal structures, phase transformations, EOSs, and other thermodynamic properties is a major focus of static high-pressure studies (Duffy, 2005). Significant changes in atomic bonding occur at high pressures, and materials also undergo major changes in mechanical and rheological properties.

At present, the DAC can sample most of the P–T range expected in the Earth's interior. Further development of diamond cell technology promises to expand the available pressure range further and, equally importantly, expand the types and accuracy of experiments that can be performed. Yet, it is unlikely that DAC techniques will be able to reach the full range of P–T conditions that are expected to be encountered in super-Earth exoplanets (**Figures 4** and **5**). For higher-pressure experiments, dynamic compression techniques are required.

2.07.3.2.2 Dynamic compression

Shock compression is the major technique used for achieving high pressures dynamically. Shock wave studies have wide applications to understanding high-pressure behavior, impact phenomena, and the high-strain rate response of all types of materials. A review of shock compression studies for planetary applications is given by Ahrens (1987) and in **Chapter 2.16**. A shock wave is a large-amplitude mechanical wave across which pressure, density, particle velocity, temperature, and other material properties change nearly discontinuously (Boslough and Asay, 1993; **Figure 8**). Shock waves propagate with supersonic velocity (relative to unshocked material), and unlike acoustic waves, their velocity is amplitude-dependent. For shock waves that propagate in a steady manner, the Rankine–Hugoniot equations express conservation of mass, momentum, and energy across the shock discontinuity:

$$\frac{\rho}{\rho_0} = \frac{U_S}{U_S - u_p} \quad [6]$$

$$P - P_0 = \rho_0 U_S u_p \quad [7]$$

$$E - E_0 = \frac{1}{2}(P + P_0)(1/\rho_0 - 1/\rho) \quad [8]$$

where U_S is the shock wave velocity, u_p is the particle velocity, E is the specific internal energy, and the subscript 0 refers to the initial unshocked state.

Shock compression is highly irreversible, and a substantial portion of the energy in a shock wave goes into raising the

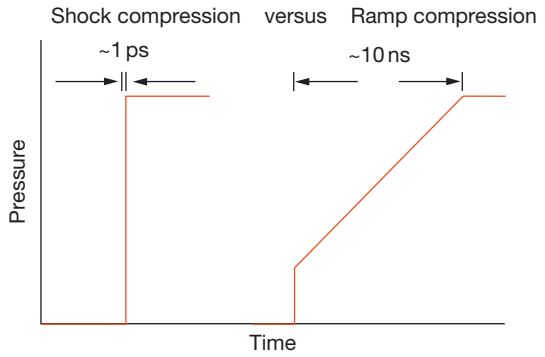

Figure 8 Schematic illustration of a shock wave (left) and a ramp wave (right). The ramp loading wave consists of an initial shock, followed by ramp loading to higher pressures. Modified from Nellis WJ (2007) Adiabat-reduced isotherms at 100 GPa pressures. *High Pressure Research* 27: 393–407, with permission.

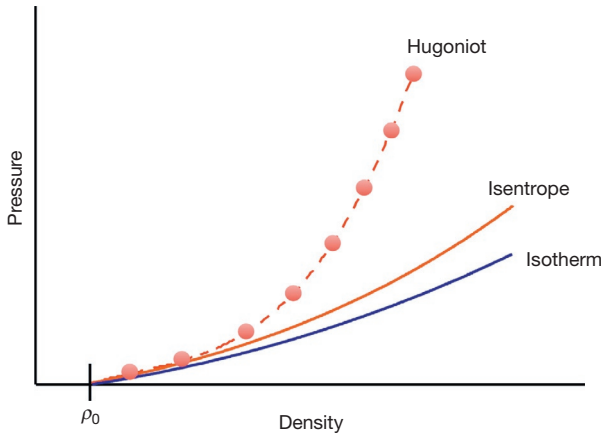

Figure 9 Thermodynamic curves for high-pressure experiments illustrating the isotherm (diamond anvil experiments), isentrope (approached by ramp compression), and Hugoniot (shock wave experiments). Ramp compression can sample the P–T–ρ space between the principal isentrope and the shock Hugoniot curve.

entropy of the material. As a result, temperature rises with compression. At low pressure, the temperature rise is modest, but temperature increases strongly at higher compression. Shock heating ultimately leads to melting of solids. This typically occurs at pressures of ~100–300 GPa for refractory materials of planetary interest, so shock wave experiments at ultrahigh pressures are probing high-temperature liquid states. There is also a limiting value to the achievable compression as the shock energy becomes increasingly partitioned into additional heating of the sample rather than compression (Johnson, 1999).

Standard shock wave techniques use gas guns to accelerate a flyer plate to several km s^{-1}, which generates a shock wave when impacting a sample. The shock and particle velocities are measured using laser interferometry or a streak camera. This enables the thermodynamic state (P, ρ, and E) to be constrained through application of the Rankine–Hugoniot equations (eqns [6]–[8]). As shown in Figure 9, the Hugoniot curve is the locus of final states achieved with a single shock from a given set of initial conditions (note that it is not the thermodynamic path followed by the shocked material). Each shock compression experiment thus determines a single datum on the Hugoniot curve. An important consequence of eqns [6]–[8] is that an independent pressure calibrant is not required for shock experiments as pressure is determined from the measured flow variables and conservation of momentum. For this reason, reduced shock wave data are commonly used for the calibration of pressure standards in static DAC experiments (Nellis, 2007). Note also that the Hugoniot equations do not constrain temperature directly, but this can be obtained in many cases by a measurement of the thermal radiation emitted by the shocked sample (Eggert et al., 2009; Luo et al., 2004; Svendsen and Ahrens, 1987).

In addition to gas-gun experiments, high-powered lasers and magnetic pulsed power facilities are increasingly being used for dynamic loading of materials. There are several large laser facilities worldwide including the VULCAN laser, an eight-beam 2.5 kJ Nd: glass laser at the Rutherford Appleton Laboratory (Danson et al., 1998; Ross et al., 1981); the Omega laser, a 60-beam 30-kJ Nd: glass laser at the University of Rochester (Boehly et al., 1997); and the National Ignition Facility (NIF) at Lawrence Livermore National Laboratory, which is a 192-beam laser with up to 2 MJ of laser energy (Moses, 2011). In experiments at these facilities, irradiance from a short (~ns), intense laser pulse causes the surface of the sample under study to ablate, and the plasma blowoff creates a strong compression wave that propagates through the sample (Figure 10). The Z machine at Sandia National Laboratory is a pulsed power accelerator that can produce currents to 20 MA and magnetic fields to 10 MG that is also capable of ultrahigh-pressure dynamic compression experiments (Matzen et al., 2005).

Thermodynamic paths of interest for compressed states of matter are compared in Figure 9. The isotherm is the pressure–volume response of the material at constant temperature. The 300 K isotherm can be measured in a DAC experiment, whereas the 0 K isotherm or cold curve can be obtained from ground-state DFT calculations. The Hugoniot is the result of adiabatic, but highly irreversible shock compression, resulting in a high-temperature shock state and a pressure offset from the isotherm that increases with compression. At lower pressures, where shock heating is small, the Hugoniot is close to the isentrope (neglecting strength effects), but these diverge increasingly at higher pressures. The isentrope is the thermodynamic path that corresponds to continuous compression that is both adiabatic and reversible. In this case, there is a modest temperature rise resulting from compression, and the isentrope lies above the isotherm.

An alternative dynamic loading technique that is attracting interest for the study of materials under exoplanetary conditions is ramp loading (Bradley et al., 2009; Lorenz et al., 2005). In this case, the material is dynamically loaded at a slower rate corresponding to rise times of 10–100 ns, compared with ~1 ps for shock compression (Figure 8). These loading rates are sufficiently slow that isentropic, rather than shock, compression is produced at least ideally. A ramp compression wave can be viewed in the limit where the compression wave is broken up into a series of weak shocks that isentropically compress the sample up to the final pressure. In reality, there

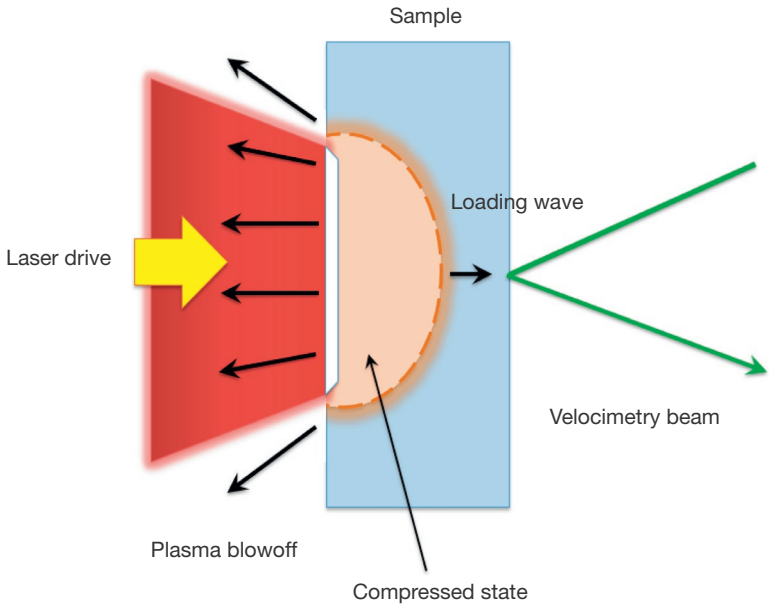

Figure 10 Schematic diagram illustrating laser-based dynamic compression experiment.

will be irreversible work and heating due to dissipative processes such defect generation and motion, and so the term 'quasi-isentropic' is sometimes used.

Ramp loading has a number of potential advantages for studying materials at ultrahigh pressures. The lower entropies achieved upon ramp loading mean that the amount of heating will be much less than for shock compression and, consequently, solids can be compressed to very high pressures without experiencing melting. It enables access to the wide range of P–T states that lie between the isotherm and the Hugoniot (Figure 9). In addition, ramp loading allows measurement of a continuum of pressure–density states along the load curve, unlike steady shock compression, which yields only one point on the Hugoniot per experiment. However, ramp loading conditions can be challenging to maintain experimentally because sound velocities normally increase with pressure, and large-amplitude pressure waves thus tend to steepen into shocks.

Ramp compression can be carried out using various techniques including projectile impact methods, pulsed magnetic sources, and high-powered pulsed lasers as described earlier for shock compression. Laser ramp compression experiments on the 30 kJ Omega laser have probed materials such as diamond, iron, and magnesium oxide to pressures as high as 900 GPa (Bradley et al., 2009; Coppari et al., 2013; Wang et al., 2013). x-Ray diffraction can also be carried out in ramp loading experiments (Rygg et al., 2012). In these experiments, a thin powder sample, held between diamond plates, is ramp- or shock-compressed using a laser source. Wave reverberations between the sample and diamond plates create a state of uniform pressure in the sample. Measurement of the velocity history of the rear diamond, together with the known EOS of diamond (Bradley et al., 2009), allows determination of the pressure history of the thin sample. A second set of lasers are used to irradiate a thin foil creating a quasimonochromatic x-ray source. The x-rays impinge on the sample through a collimating pinhole, allowing a diffraction pattern to be recorded on image plates surrounding the sample. x-Ray diffraction data on MgO have been measured to 900 GPa by this technique (Coppari et al., 2013). This provides direct determination of the pressure–density states and provides a means to directly determine crystal structures under dynamic loading at extreme conditions for the first time.

2.07.4 Equations of State

The EOS is a relationship between the pressure, temperature, and density of a material in thermal equilibrium. The $\rho(P, T)$ EOS is one of the most important high-pressure material properties and an essential component of interior structure models for exoplanets as discussed earlier (eqns [1]–[3]). For the range of plausible masses of super-Earths (1–10 M_E), the interior pressures and temperatures are expected to be very high (to ~4000 GPa, 10 000 K) (Figures 4 and 5) and require accurate characterization of the EOS over large compression. The various experimental and theoretical techniques that can be used for EOS measurements have been discussed earlier. Experimental compression data are typically fit using semiempirical EOS such as the Birch–Murnaghan or the Vinet equation. The Birch–Murnaghan EOS (Birch, 1952) is widely used in geophysics and is derived from a power series expansion of the free energy in finite strain. To the third order in Eulerian strain, the Birch–Murnaghan equation is given by

$$P = \frac{3}{2}K_0\left[\left(\frac{V_0}{V}\right)^{7/3} - \left(\frac{V_0}{V}\right)^{5/3}\right]\left\{1 + \frac{3}{4}\left[K_0' - 4\right]\left[\left(\frac{V_0}{V}\right)^{2/3} - 1\right]\right\} \quad [9]$$

where V is the volume, K is the bulk modulus, K' is the pressure derivative of the bulk modulus, $\partial K/\partial P$, and the subscript 0 refers to ambient-pressure conditions. Parameters of the EOS are typically fit using experimental data from DAC

experiments or shock compression data appropriately corrected for thermal effects. Uncertainties in the Birch–Murnaghan EOS arise from truncation of the power series (typically to the third order in strain) and the choice of finite strain measure. This equation has been used to represent the EOS in several studies of exoplanet interiors to date (Seager et al., 2007; Sotin et al., 2007; Valencia et al., 2006).

Another EOS widely used for solids is the Vinet equation (Vinet et al., 1986, 1989):

$$P = 3K_0 \frac{1-X}{X^2} \exp\left[\frac{3}{2}\left(K_0' - 1\right)(1-X)\right] \qquad [10]$$

where $X = (V/V_0)^{1/3}$. This equation is based on a Rydberg interatomic potential and is expected to be applicable to solids with a wide range of bonding types. Comparisons of EOSs with experimental and theoretical data over wide ranges of compression support the reliability of the Vinet equation for best characterizing experimental data (Cohen et al., 2000). This equation or a modified form of it has also been adopted for exoplanet interior modeling (Valencia et al., 2007b; Wagner et al., 2012). Examples of EOSs for major potential components (Fe, $MgSiO_3$, and H_2O) of super-Earths are shown in **Figure 11**.

The effects of temperature on the EOS can be included using one of several thermal models (Duffy and Wang, 1998). A particularly useful approach is the Mie–Grüneisen–Debye formulation, which uses a thermal correction to the isothermal EOS that accounts for lattice vibrations with a cutoff frequency corresponding to the Debye frequency (Jackson and Rigden, 1996). The total pressure is divided into a cold term, P_c, and a thermal term, P_{th}:

$$P(V,T) = P_c(V) + P_{th}(V,T) \qquad [11]$$

The reference isotherm, P_c, is given by an EOS such as the Vinet or Birch–Murnaghan equation. The thermal pressure is obtained from

$$P_{th} = \frac{\gamma}{V}[E(T,\theta) - E_c(T_c,\theta)] \qquad [12]$$

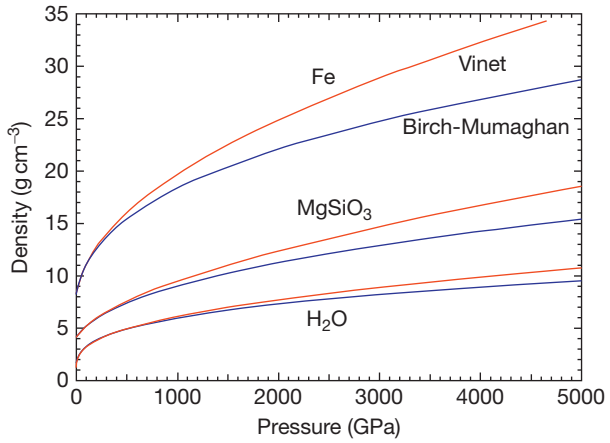

Figure 11 Room-temperature equations of state for representative planetary materials. Blue and red curves show difference in density resulting from extrapolations of experimental data using the Birch–Murnaghan and Vinet equations, respectively. Equation of state parameters for each material are from Fe (Dewaele et al., 2006), $MgSiO_3$ (Lundin et al., 2008), and H_2O (Somayazulu et al., 2008).

where E is the thermal energy, γ is the Grüneisen parameter, and θ is the Debye temperature. The thermal energy can be calculated from the Debye model:

$$E(T,\theta) = 9nRT\left(\frac{T}{\theta}\right)^3 \int_0^{\theta/T} t^3 \mathrm{d}t/(\mathrm{e}^t - 1) \qquad [13]$$

where n is the number of atoms per formula unit and R is the gas constant. The Debye temperature and Grüneisen parameters are functions of volume according to

$$\gamma(V) = \gamma_0\left(\frac{V}{V_0}\right)^q \qquad [14]$$

and

$$\theta = \theta_0 \exp\left[(\gamma_0 - \gamma(V))/q\right] \qquad [15]$$

where q controls the volume dependence of γ. The complete Mie–Grüneisen–Debye equation thus requires specification or determination of six parameters: V_0, K_0, K_0', γ_0, θ_0, and q. The thermal parameters can be obtained from P–V–T experimental data or from measurements or estimates from elasticity or other thermodynamic data (Duffy and Wang, 1998; Jackson and Rigden, 1996). Under super-Earth conditions, the effect of temperature on density is considered to be of second-order importance compared to the pressure effect (Seager et al., 2007; Valencia et al., 2007a), so the thermal EOS only plays a minor role in determining the mass–radius relationship. The thermodynamic properties, however, are essential for thermal and evolutionary models of exoplanets (e.g., Wagner et al., 2012). The Grüneisen parameter plays a particularly important role. Interior temperatures in super-Earths are expected to be sufficiently hot that thermal convection will be a dominant heat transport mechanism. For a convecting super-Earth, the adiabatic temperature gradient, $(\partial T/\partial r)_S$, is given by

$$\left(\frac{\partial T}{\partial r}\right)_s = -\frac{\rho g \gamma T}{K_S} \qquad [16]$$

where r is the planetary radius, g is gravitational acceleration, and K_S is the adiabatic bulk modulus. While absolute temperatures of a planet will depend on many factors as discussed previously, the adiabatic gradient determines the slope of the temperature profile for convecting regions in the mantle and core. The Grüneisen parameter is also used to estimate the melting temperatures of mantle and core materials through Lindemann's law (Gaidos et al., 2010; Poirier, 2000; Stamenkovic et al., 2011; Valencia et al., 2006).

Another P–V–T EOS that has been used for modeling exoplanets is ANEOS (Thompson, 1990; Thompson and Lauson, 1972), which is a long-standing EOS widely used in the modeling of shock experiments and impact events. It uses a thermodynamically consistent Helmholtz free energy formulation that extrapolates to the Thomas–Fermi limit (discussed in the succeeding text) at ultrahigh pressures. ANEOS is largely based on experimental shock wave data with thermal corrections using the Grüneisen parameter. An advantage of this EOS is the correct asymptotic behavior at very high pressures, but potential limitations include its approximate treatment of phase transitions, large thermal corrections from Hugoniot conditions to the high-P, lower-T conditions of planetary interiors, and limited options for modeling geological materials (Melosh, 2007). However, a

recent comparison of EOSs for exoplanet applications concluded that ANEOS does work well in the pressure regime of particular interest for exoplanet interiors (Grasset et al., 2009).

Since EOSs must be extrapolated to very high pressures beyond the range of experiments, their reliability at high compressions must be evaluated. Stacey (2000) suggests that K'_∞, the asymptotic limit of the pressure derivative of the bulk modulus as pressure goes to infinity, can be used as an additional criterion for evaluating EOSs. A constraint on K'_∞ obtained from thermodynamic relationships at this infinite limit can be used to modify the Vinet equation to be consistent with this limit (Stacey and Davis, 2004). At extreme pressures, all materials are expected to reach the Thomas–Fermi limit of a free electron gas with embedded nuclei. In this case, the pressure of the degenerate electron gas is calculated using the TFD approximation. TFD-based electronic structure theory (Salpeter and Zapolsky, 1967) is expected to provide an adequate EOS at pressures exceeding ~10 TPa (Grasset et al., 2009; Seager et al., 2007). Uncertainty in the EOS therefore is primarily in the regime between 0.2 and 10 TPa, beyond the limit of most experimental data and below the validity of the high-density, fully ionized limit. Existing EOSs for planetary materials can differ by ~20–30% in the 100 GPa to 10 TPa range (Baraffe et al., 2008). Comparisons of models with different EOSs suggest that uncertainty in EOS translates into an uncertainty in radius of ~2–3% for a given mass planet (Fortney et al., 2009; Wagner et al., 2011). As this uncertainty is comparable to the expected precision in future telescope observations of transits, reducing EOS uncertainty is needed to make structure models more accurate.

2.07.5 Mineralogy at Super-Earth Interior Conditions

2.07.5.1 Composition of Super-Earths

The bulk composition of a planet should reflect that of its host star as modified by planet-forming processes within the protoplanetary disk. In general, a wide range of bulk compositions for terrestrial-type planets should be possible, in principle. The mineralogy of terrestrial super-Earths can be modeled assuming an Earth-like composition as a starting point. The composition of Earth is dominated by O, Fe, Mg, and Si with lesser amounts of Ca and Al (McDonough and Sun, 1995). The Earth's interior consists of a mantle composed of Mg-rich silicates and oxides overlying a metallic Fe core, with other species in minor amounts (see **Chapters 2.03**, **2.06**, and **10.02**).

Measured photospheric stellar abundances of the elements provide constraints on both internal and atmospheric compositions of exoplanets as well as insights into what characteristics of protoplanetary clouds favor planetary formation (Delgado Mena et al., 2010). The Mg/Si, Fe/Si, and C/O ratios are important for determining the mineralogy and structure of terrestrial planets. The Mg/Si ratio will control the relative abundance of the major silicates such as pyroxenes (Mg/Si = 1) and olivine (Mg/Si = 2). The solar and bulk Earth Mg/Si values are close to one (Asplund et al., 2009; Kargel and Lewis, 1993; McDonough and Sun, 1995). Photospheric measurements of planet-hosting stars show a range of Mg/Si values ranging from ~0.7 to ~1.4 (Delgado Mena et al., 2010). In simulations of planetary formation that included variable chemical composition in the protoplanetary disk, terrestrial planets with variable compositions, some very different from Earth, were found (Bond et al., 2010). Models of systems with low Mg/Si ratios yield planets that are Mg-depleted compared to Earth and are formed from silicates such as pyroxenes and feldspars (Carter-Bond et al., 2012a). However, studies of the relationship between solar abundances, meteorites, and Earth bulk compositions have shown that the relationship between planetary compositions and stellar abundances is complex (Drake and Righter, 2002).

The bulk Fe/Si ratio is an important parameter for determining the size of the metallic core in a terrestrial exoplanet. Values of core mass fraction used in typical models to date are based on analogy to our solar system and range from Earth-like (~33%) to Mercury-like (~66%), while end-member models ranging from pure core to a silicate-only coreless planet are useful for delineating the range of mass–radius space potentially occupied by rocky planets. The core mass fraction will depend not only on bulk Fe content but also on core formation processes that partition Fe between mantle and core (Elkins-Tanton and Seager, 2008). It may also be affected by loss of a planet's mantle due to large impacts or evaporation due to stellar irradiation. For planets of our solar system, the Mg# (=molar Mg/Mg+Fe) of the mantle is known for only Earth and Mars and ranges between 0.7 and 0.9. The distribution of Fe between mantle and core has little overall effect on the mass–radius relationship (Elkins-Tanton and Seager, 2008; Fortney et al., 2009).

The presence of water or other hydrous phases in a terrestrial-type planet is of particular interest as an essential component of habitability. The presence of water can also affect melting behavior and rheology and may affect the likelihood of plate tectonics (Korenaga, 2010). Migration of giant planets may greatly increase the efficiency of delivery of water and hydrous phases to growing terrestrial planets even promoting formation of ocean planets and wet Earths (Carter-Bond et al., 2012b). Close proximity to the host star, on the other hand, can lead to intense heating, which would be expected to strip volatiles from the planet.

Long-lived radioactive elements (^{40}K, ^{232}Th, ^{235}U, and ^{238}U) play an important role as internal heat sources in the Earth, controlling internal temperatures and thermal evolution. The amount of internal heating relative to basal heating in the mantle will affect both internal and surface dynamics (van Heck and Tackley, 2011). Most models of extrasolar planets to date have assumed chondritic abundances of these elements (Tachinami et al., 2011), but the range of possible variability is poorly constrained. Ice-rich planets may be significantly cooler in the interior compared to rocky planets of the same mass due to reduced abundance of radioactive elements (Sotin et al., 2007).

The C/O ratio is a chemical parameter that controls the distribution of Si among oxides and carbides (Bond et al., 2010). Under equilibrium conditions in the innermost region of the protoplanetary disk, a C/O value <0.8 leads to interiors dominated by silicates (**Figure 12**). When the C/O ratio is >0.8, Si exists as SiC with additional C also present. Further out in the disk, silicates dominate but the resulting planets can be carbon-rich. The types of rocky planets that may form under high C/O ratios have been classified as carbon planets

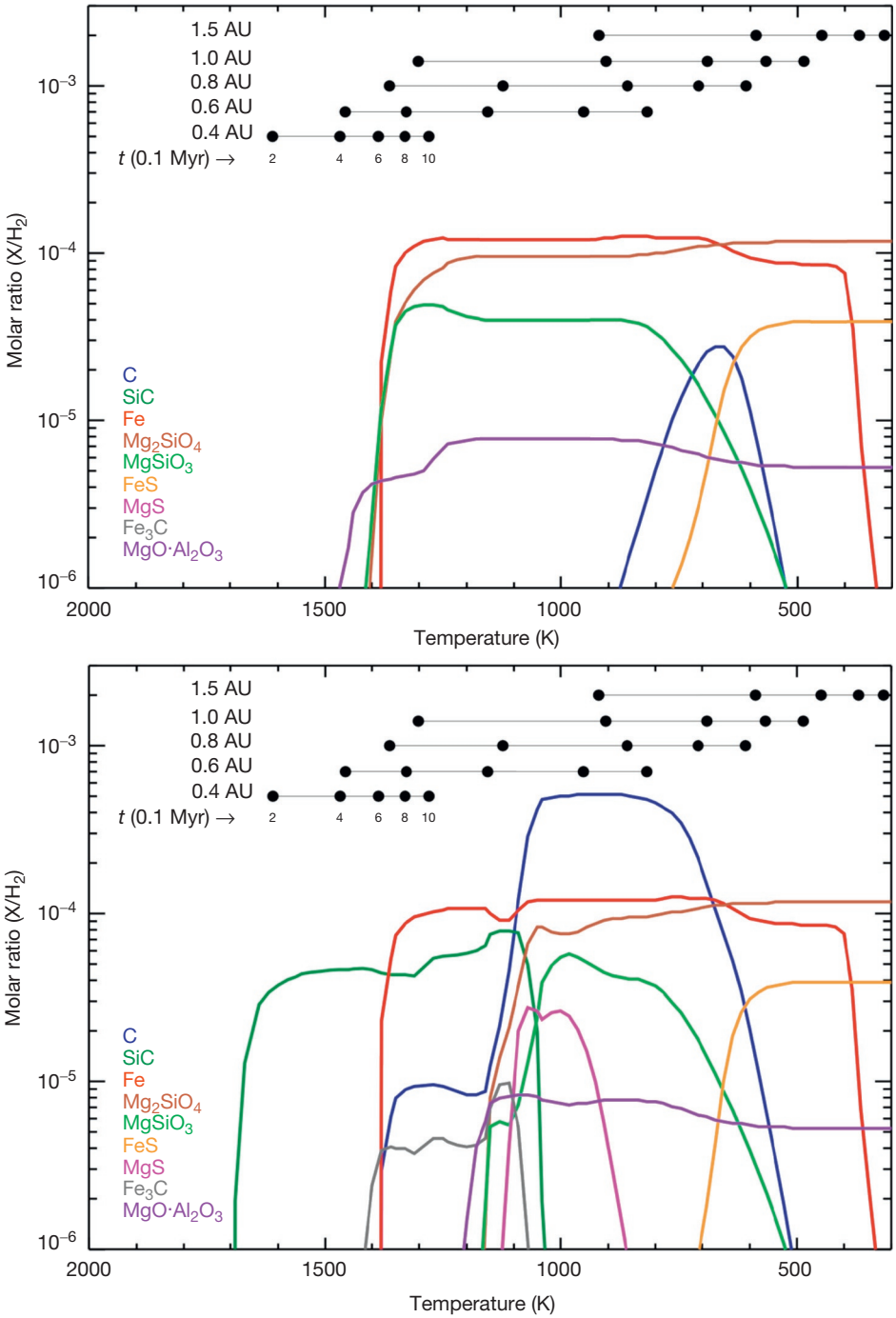

Figure 12 Chemical composition of refractory condensates expected in the protoplanetary disk of the Sun (C/O ratio = 0.54) (top) and of the 55 Cancri system (C/O ratio = 1.12) (bottom). The colored curves show molar mixing ratios of the major species, shown in the legend, in thermochemical equilibrium as a function of temperature in the protoplanetary disk midplane. A representative pressure of 10^{-4} bar is assumed. The elemental abundances of the host star (Carter-Bond et al., 2012b; Delgado Mena et al., 2010) are assumed as initial conditions, and the equilibrium computations were performed using thermochemical software (HSC Chemistry). The black filled circles at the top of the figure show the temperatures of the disk at different orbital separations and ages. Reproduced from Madhusudhan N, Lee KKM, Mousis O (2012) A possible carbon-rich interior in super-Earth 55 Cancri e. *Astrophysical Journal Letters* 759(2): L40. http://dx.doi.org/10.1088/2041-8205/759/2/L40, with permission.

(Kuchner and Seager, 2005). A wide range of C/O values have been observed in the photospheric abundances of exoplanet host stars with about one-third of planet-hosting stars having C/O values >0.8 (Delgado Mena et al., 2010; see also Petigura and Marcy, 2011). On the other hand, some recent studies have suggested that previous determinations of high C/O in stars could have been overestimated due to systematic errors in estimating the C and O abundances and that carbon-rich main-sequence stars, and hence carbon planets, would be rare (Fortney, 2012; Nissen, 2013).

2.07.5.2 Crystal Structures and Phase Transitions in Minerals at Ultrahigh Pressures

The Earth's mantle extends to a depth of ~2900 km and reaches a maximum pressure of ~135 GPa (Dziewonski and Anderson, 1981). The upper mantle above 660 km depth is composed mainly of the minerals olivine, pyroxene, and garnet. These minerals undergo a series of phase transitions to denser structures under upper mantle conditions. The major discontinuity at 660 km depth is due to a series of phase transitions culminating in formation of $(Mg,Fe)SiO_3$ perovskite and (Mg,Fe)O ferropericlase, the two most abundant phases in the lower mantle. Mg-perovskite undergoes a further transformation to the $CaIrO_3$-type postperovskite structure near the base of the mantle, a few hundred km above the core. The other main mineral of the lower mantle is $CaSiO_3$ perovskite. The composition of the bulk of the lower mantle, by volume, is expected to be about 70% Mg-perovskite, 20% ferropericlase, and 10% Ca-perovskite (see Chapter 2.03).

The Earth's core accounts for approximately one-third of Earth's mass. Cosmochemical and geophysical evidence indicates that the core not only is mostly iron but also contains Ni and about 10% by mass of a lighter element. The candidates for the major light element of the core are S, O, Si, C, and H, but it is not yet certain which of these is dominant. The core is divided into a small, solid inner core (about 2% of Earth's total mass) and a larger, liquid outer core. The inner core grows slowly over time as the Earth cools. The inner core contains fewer light elements than the outer core, and thus, the composition of the outer core is becoming slowly enriched with lighter elements over time as the inner core grows. This partitioning of lighter elements during inner core crystallization is an important contributor to the driving forces for convective motion of the outer core fluid from which the Earth's magnetic field is generated. For more details on the core, see Chapter 2.06.

The internal mineralogy of super-Earths will depend on the composition of each planetary layer and pressure and temperature. Here, we review the current understanding of mineralogy and crystal structures of likely phases of relevance. For terrestrial super-Earths, we focus on simple oxides and silicates: MgO, FeO, CaO, Al_2O_3, SiO_2, and $MgSiO_3$ (Figure 13). Properties of the end-member oxides are an important starting point to understand solid solution, solubility, and dissociation reactions in plausible mineral assemblages. Even for these simple compositions, the phase diagrams are only beginning to be explored at the high P–T conditions characteristic of super-Earth and exoplanet interiors. The behavior of Fe and Fe alloys relevant to the high-pressure conditions expected in super-Earth cores will also be reviewed. The behavior of carbon, H_2O, and other ices is also relevant given the possible range in super-Earth composition extending from terrestrial to Neptune-like planets. C and H_2O are, of course, of special interest due to their importance for addressing questions of habitability and the existence of life. The behavior of all these materials at ultrahigh pressures is not only of interest for super-Earths but also relevant to understanding the cores of giant planets (Chapter 10.16), both in our solar system and beyond.

2.07.5.2.1 MgO

MgO (periclase) is the end-member of the (Mg,Fe)O solid solution. Its high-pressure behavior has attracted much attention due to its simple structure, wide stability field, and geophysical importance. MgO crystallizes in the B1 rock-salt structure, and static compression experiments have shown that the B1 phase remains stable to at least 250 GPa

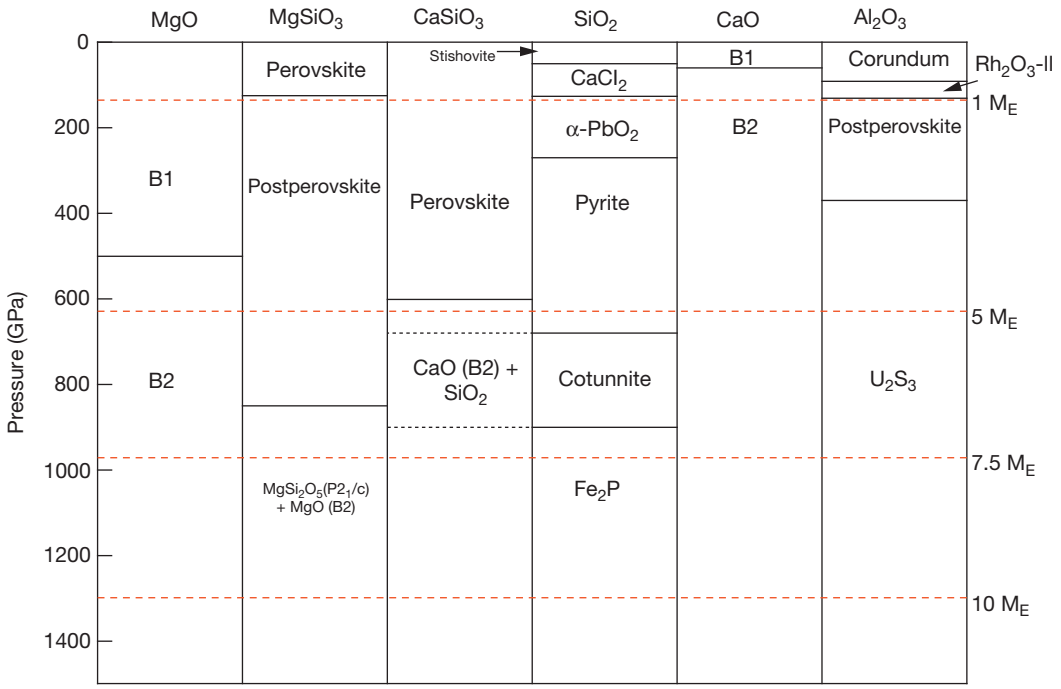

Figure 13 Phase transitions in selected terrestrial mantle constituents at ultrahigh pressures. Red dashed lines show expected core–mantle boundary pressure for terrestrial super-Earths of different sizes based on the model of Wagner et al. (2012).

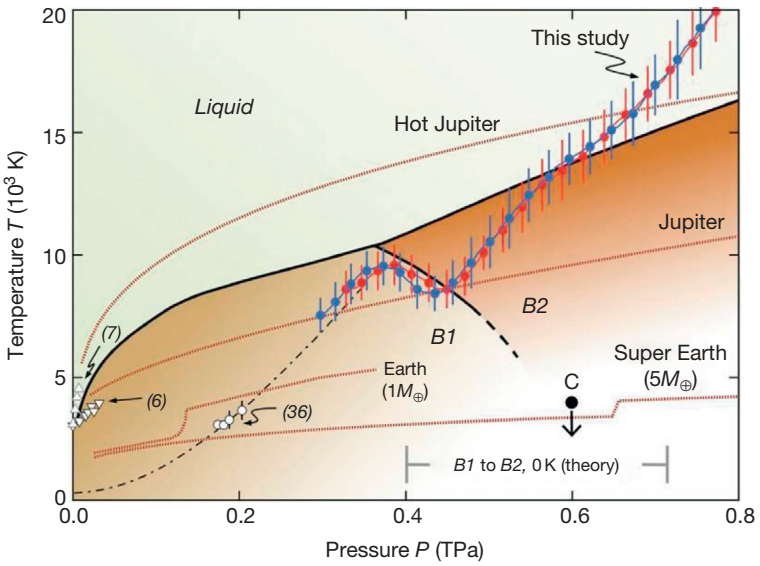

Figure 14 Phase diagram of MgO. Filled red and blue circles and corresponding curves are the shock pressures and temperatures from laser experiments. Brown lines show expected *P–T* paths for Earth, a 5 M_E super-Earth, Jupiter, and a hot Jupiter. The melting curve and B1–B2 phase transition boundary are also indicated. The filled circle labeled C shows the pressure and upper bound temperature for the B1–B2 transition from ramp compression x-ray diffraction experiments (Coppari et al., 2013). Adapted from McWilliams RS, Spaulding DK, Eggert JH, et al. (2012) Phase transformations and metallization of magnesium oxide at high pressure and temperature. *Science* 338(6112): 1330–1333. http://dx.doi.org/10.1126/science.1229450, with permission.

(Dorfman et al., 2012; Duffy et al., 1995). Experimental and theoretical constraints on the MgO phase diagram are summarized in **Figure 14**. Theoretical calculations predict a transformation to the B2 CsCl-type structure with an increase in Mg coordination from 6 to 8 around 400–600 GPa at 0 K (Alfe et al., 2005; Belonoshko et al., 2010; Karki et al., 1997a; Mehl et al., 1988; Oganov et al., 2003; Strachan et al., 1999). A negative Clapeyron slope is predicted theoretically for this phase boundary (Belonoshko et al., 2010; Oganov et al., 2003; Strachan et al., 1999). Ab initio random structure searching has been applied to MgO over 1000–4000 GPa, and no other structure was found to be competitive in enthalpy with the CsCl structure at 0 K (Wilson and Militzer, 2012). Theoretical DFT calculations have also predicted that solid MgO metallizes at 0 K at very high pressures (2100 GPa) (Oganov et al., 2003).

Shock compression work on MgO has reached pressures as high as 1400 GPa (Fat'yanov et al., 2009; McWilliams et al., 2012; Svendsen and Ahrens, 1987; see also **Chapter 2.16**). A possible phase transition in MgO was identified in gas-gun shock experiments at ~170 GPa (Zhang et al., 2008), but the nature of this transformation is poorly constrained. At higher pressures, laser-shock measurements of the EOS, temperature, and optical reflectivity reveal two temperature discontinuities, which are interpreted as the B1–B2 phase transformation at ~400 GPa and 9000 K and melting at ~650 GPa and 14 000 K (McWilliams et al., 2012). Based on optical reflectivity measurements, the liquid is metallic at these conditions. x-Ray diffraction measurements on ramp-compressed MgO have directly detected the B1–B2 phase transition at ~600 GPa (Coppari et al., 2013). The observed transition pressure under ramp loading is consistent with both theoretical calculations and shock wave data given the expected negative *P–T* Clapeyron slope of the transition. The x-ray measurements further show that the B2 phase also remains stable to a peak pressure of 900 GPa, the highest-pressure x-ray diffraction data yet reported on any solid (Coppari et al., 2013).

The melting curve of MgO at ~Mbar pressures is controversial with a large discrepancy between experimental and theoretical determinations (Alfe, 2005; Belonoshko et al., 2010; Strachan et al., 1999; Tangney and Scandolo, 2009; Zerr and Boehler, 1994; Zhang and Fei, 2008). The recent laser-shock temperature measurements (McWilliams et al., 2012) indicate that melting occurs much higher than the *P–T* conditions for Hugoniot melting predicted from first-principles MD calculations (de Koker and Stixrude, 2009). A recent study of the Mg–O system using ab initio structure search methods up to 850 GPa found, in addition to MgO, that two additional compounds, MgO_2 and Mg_3O_2, become stable at 116 and 500 GPa, respectively (Zhu et al., 2013).

2.07.5.2.2 FeO

Wüstite, $Fe_{1-x}O$, is of importance for both the mantles and the cores of terrestrial planets. As discussed earlier, the (Mg,Fe)O solid solution is a major component of terrestrial mantles. The amount of FeO in the mantle affects the electrical and thermal conductivity of the region. FeO can also be a major alloying component of the core. Phase relations in FeO are shown in **Figure 15**. At lower temperatures, wüstite undergoes transformations from the B1 structure to a distorted structure and then to the B8 (NiAs-type) structure at Mbar pressures (Fei and Mao, 1994). At high temperatures, the B1 phase undergoes an insulator to metal transformation at ~70 GPa (Fischer et al., 2011; Gramsch et al., 2003; Ohta et al., 2012a). As a result, a miscibility gap would be expected to form in the (Mg,Fe)O system at

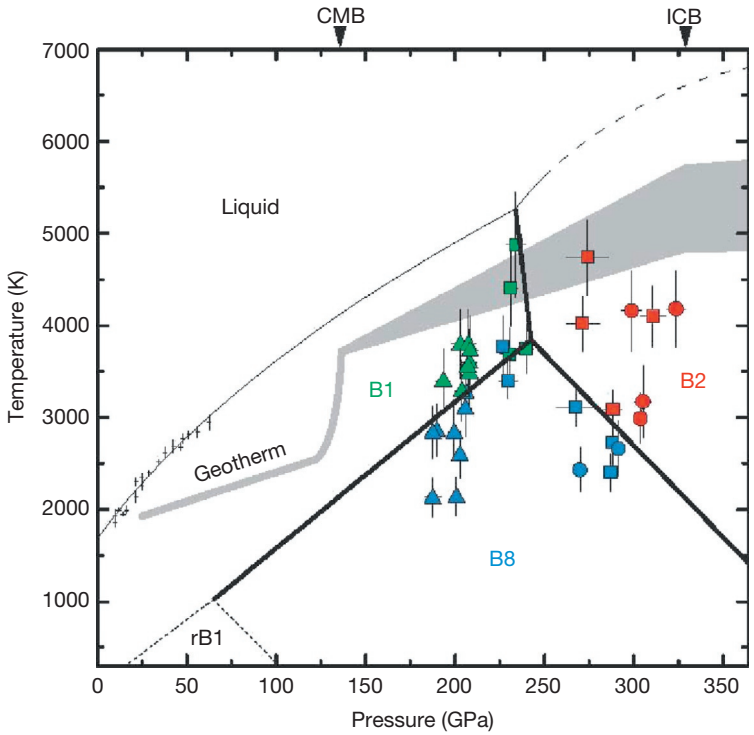

Figure 15 Phase diagram of FeO showing boundaries for B1, B2, B8, and rhombohedral phase (rB1). The melting curve and a representative geotherm for Earth are also indicated. CMB and ICB designate Earth core–mantle boundary and inner core boundary, respectively. Reproduced from Ozawa H, Takahashi F, Hirose K, Ohishi Y, and Hirao N (2011) Phase transition of FeO and stratification in Earth's outer core. *Science* 334(6057): 792–794. http://dx.doi.org/10.1126/science.1208265, with permission.

high pressures. The metallic behavior of FeO should also allow oxygen to dissolve more readily into metallic cores. B1 FeO eventually transforms to the B2 structure at 240 GPa (and ~4000 K) (Ozawa et al., 2011), compared with ~600 GPa for MgO (Coppari et al., 2013). The variation of the B1–B2 transition pressure for intermediate (Mg,Fe)O compositions is unknown. The melting curve of FeO has been measured to 77 GPa and 3100 K (Fischer and Campbell, 2010).

2.07.5.2.3 SiO_2

Silica is the most abundant oxide component of terrestrial mantles and serves as an archetype for the dense highly coordinated silicates of planetary interiors. While free SiO_2 is only expected in localized regions in Earth's mantle such as subducted oceanic crust, the wider range of plausible compositions and higher P–T conditions in super-Earth exoplanets allow for greater possible presence of silica phases in terrestrial exoplanets. The stability of silicate phases may be affected by polymorphism in SiO_2, and silicate disproportionation could produce silica-rich regions in deep interiors.

Over the pressure range of the Earth's crust and mantle, SiO_2 undergoes a well-known sequence of phase transitions (**Figure 16**). Quartz transforms first to coesite and then to octahedrally coordinated stishovite above ~10 GPa. At ~50 GPa, stishovite transforms to the orthorhombic $CaCl_2$-type structure (Kingma et al., 1995; Tsuchida and Yagi, 1989). SiO_2 undergoes a further transformation to the α-PbO_2-type structure at pressures near those of the Earth's core–mantle boundary region (Karki et al., 1997b; Murakami et al., 2003). The highest-pressure transformation yet observed experimentally is to the pyrite-type structure (with 6+2 coordination of oxygen around Si^{4+}) at around 270 GPa (Kuwayama et al., 2005).

Further phase transformations of SiO_2 have been explored using theoretical calculations and analog systems. DFT predictions of transformation of SiO_2 to a cotunnite-type phase around 690–750 GPa (at 0 K) have been reported (Oganov et al., 2005; Umemoto et al., 2006a). This involves a large increase in Si^{4+} coordination from 6+2 (pyrite) to ninefold coordination (cotunnite). However, more recent theoretical calculations have reported that instead, the hexagonal Fe_2P-type phase is the stable phase of SiO_2 above 700 GPa and 0 K (Tsuchiya and Tsuchiya, 2011; Wu et al., 2011). This phase has been also predicted to occur in TiO_2 and GeO_2 and has now been observed experimentally in TiO_2 (Dekura et al., 2011a,b).

Due to the change in coordination, the volume change associated with the post-pyrite transition is predicted to be large (~4–5%) (Tsuchiya and Tsuchiya, 2011). The high-temperature behavior of the new SiO_2 phases was explored using the QHA (Tsuchiya and Tsuchiya, 2011; Wu et al., 2011). The transformation to a postpyrite phase in SiO_2 is found to have a negative Clapeyron slope due to the increase in bond lengths and coordination number resulting in an increase in vibrational entropy across the transition (Wu et al., 2011). At low temperatures, SiO_2 transforms from the pyrite-type to the Fe_2P phase, whereas at higher

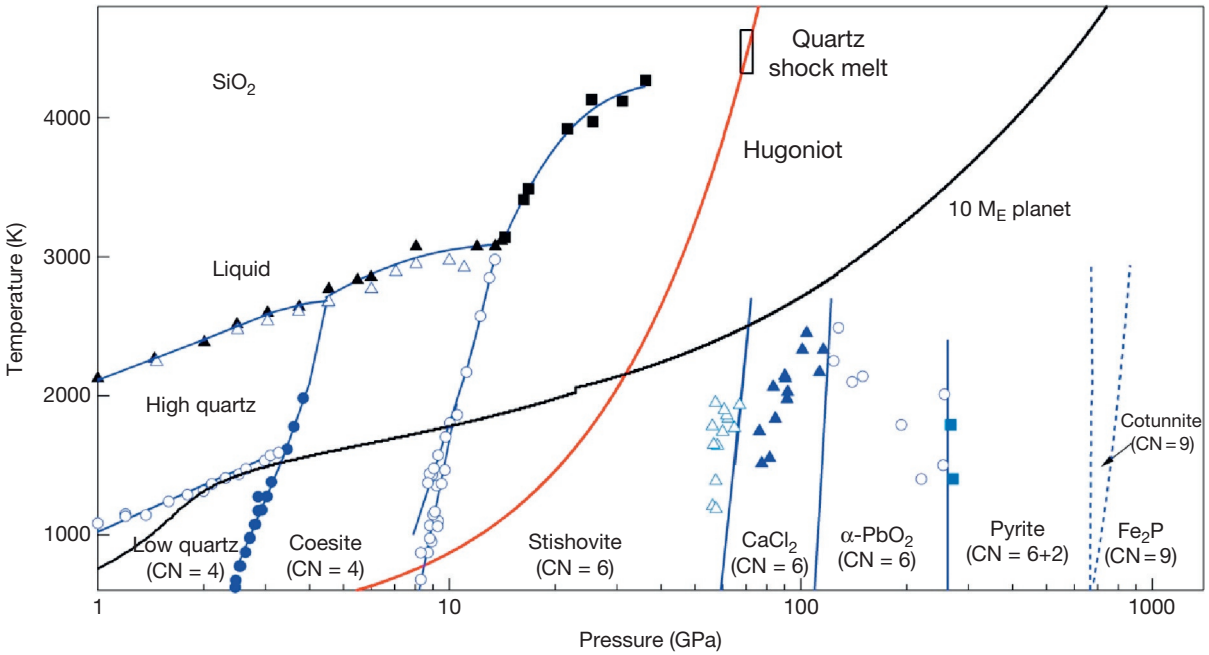

Figure 16 Phase diagram of SiO_2 showing the sequence of phase transitions up to 1000 GPa. Solid lines show experimentally determined phase boundaries, and dashed lines show theoretical boundaries for highest-pressure phases. Symbols indicate experimentally measured points along the phase boundaries. The Hugoniot curve is indicated in red with the melting point shown. A representative *P*–*T* path for a 10 M_E planet is shown.

temperatures, the pyrite phase first transforms to the cotunnite-type phase followed by a second transformation to the Fe_2P phase (with <1% volume change). The transformation from Fe_2P-type to cotunnite-type phase is expected to have a positive Clapeyron slope. Along the possible *P*–*T* path for a super-Earth, the pyrite–cotunnite transformation is expected to occur for planets of approximately 5 M_E or greater. The cotunnite–Fe_2P transformation would be expected in planets of ~7 or more M_E. Cotunnite-type SiO_2 at super-Earth interior conditions is predicted to have electrical conductivities close to metallic values (Umemoto et al., 2006a).

The high-pressure behavior of SiO_2 has also been explored extensively using dynamic experiments (see **Chapter 2.16**). Shock compression data for fused silica and quartz up to 200 GPa are interpreted as indicating transitions to stishovite and/or stishovite-like phase(s) with melting occurring above 120 GPa along the Hugoniot (Akins and Ahrens, 2002; Lyzenga et al., 1983). Measurement of the Hugoniot EOS has been extended up to 1600 GPa in recent experiments at the Sandia Z facility (Knudson and Desjarlais, 2009). Shock temperature measurements up to 1000 GPa show evidence for pronounced changes in the structure of liquid SiO_2 including dissociation and enhanced electron mobility (Hicks et al., 2006). A study of the shock vaporization of silica has recently been conducted yielding a wide ranging EOS that can be applied to better understand and potentially detect giant impacts in extrasolar planetary systems (Kraus et al., 2012).

2.07.5.2.4 $MgSiO_3$

$MgSiO_3$ in Earth's lower mantle crystallizes in the perovskite structure except for a thin layer of postperovskite near its base (Tronnes, 2010; see also **Chapter 2.03**). The higher internal pressures of large terrestrial-type exoplanets mean that the postperovskite phase should play a large or even dominant role in the interiors of these bodies (**Figure 17**; Valencia et al., 2007a; Wagner et al., 2012). Silicate perovskite and postperovskite also to incorporate iron (see **Chapter 2.03**) with the distribution of Fe among phases in the lower mantle are controlled by partitioning between $(Mg,Fe)SiO_3$ and (Mg,Fe)O (Tronnes, 2010). Iron in mantle minerals may undergo spin transitions at high pressure that may have important effects on the stability and other properties of silicate and oxide phases (Badro et al., 2004; Lin et al., 2013).

Experimental studies have demonstrated the stability of the postperovskite structure in $(Mg,Fe)SiO_3$ to pressures approaching 200 GPa, although some evidence for modifications of the structure has been reported (Yamanaka et al., 2012). Germanates are known to be good analogs for silicates, with similar sequences of phase transitions occurring at lower pressures due to the larger ionic radius of Ge^{4+} compared with Si^{4+}. The phase stability and EOS of $MgGeO_3$ have been studied to 200 GPa in the DAC, and the postperovskite phase remains stable until at least this pressure (Kubo et al., 2006). Fluorides including $NaMgF_3$, $NaNiF_3$, and $NaCoF_3$ are also expected to be good analogs for $MgSiO_3$ due to their close similarity in structural properties (Dobson et al., 2011; Duffy, 2008). High-pressure experiments and theoretical calculations on $NaMgF_3$ yield conflicting results with one experimental study reporting evidence for transformation to an unknown $NaMgF_3$ structure above 30 GPa (Martin et al., 2006) and another reporting the stability of $NaMgF_3$ postperovskite to at least 70 GPa and 2500 K (Grocholski et al., 2010). These contrast with

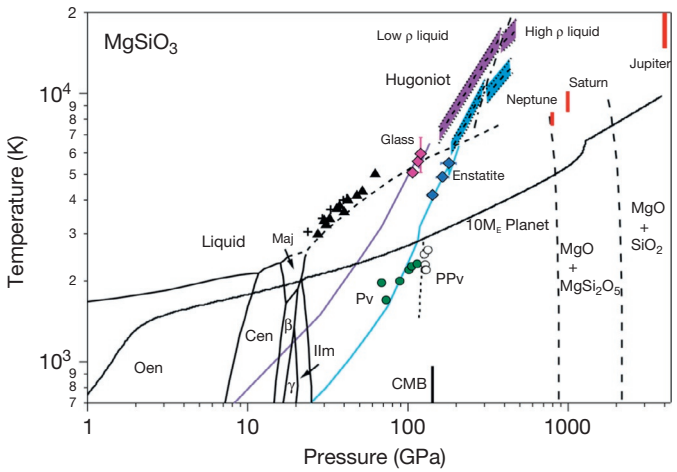

Figure 17 Phase diagram of $MgSiO_3$ showing sequence of phase transitions up to 2000 GPa. Blue and purple curves show shock Hugoniot for $MgSiO_3$ crystals (enstatite) and glass, respectively, with blue and purple diamonds showing representative gas-gun data. The black dashed lines with blue- and purple-shaded regions show laser-shock data indicating the presence of density discontinuity in the liquid regime. Experimental data are also shown for the melting curve (black symbols) and Pv–PPv boundary (green and open circles). Estimated *P–T* conditions for a 10 M_E super-Earth and cores of Jupiter, Saturn, and Neptune are indicated. Oen, orthoenstatite; Cen, clinoenstatite; β, wadsleyite + SiO_2; γ, ringwoodite + SiO_2; ilm, ilmenite; Maj, majorite; Pv, perovskite; PPv, postperovskite; CMB, Earth's core–mantle boundary.

theoretical calculations that predict the disproportionation of $NaMgF_3$ postperovskite into NaF and MgF_2 above about 40 GPa (Umemoto et al., 2006b).

Shock compression studies of $MgSiO_3$ have extended to as high as 950 GPa (Mosenfelder et al., 2009; Spaulding et al., 2012; see also **Chapter 2.16**). Laser-shock experiments have reported evidence for a liquid–liquid phase transition in $MgSiO_3$ melt at 300–400 GPa and 10 000–16 000 K with a large volume change of ~6% (Spaulding et al., 2012; **Figure 17**). A recent theoretical study has suggested that this transition may instead represent decomposition into solid MgO and liquid SiO_2 (Boates and Bonev, 2013). Measurements of optical reflectivity suggest that the melt is metallic at temperatures above ~12 000 K (Spaulding et al., 2012).

Initial theoretical calculations examining the stability of $MgSiO_3$ perovskite to ultrahigh pressures predicted that $MgSiO_3$ postperovskite breaks down into an oxide mixture of MgO (B2 phase) and SiO_2 (cotunnite-type phase) at ~1100 GPa (Umemoto et al., 2006a). However, this work did not consider the more recently discovered hexagonal Fe_2P phase of SiO_2 or possible dissociation of ABO_3 compounds into AO and AB_2O_5 (Okada et al., 2011; Wu et al., 2009) or AO and AB_3O_7 (Nishio-Hamane et al., 2012). More recent theoretical calculations predict that $MgSiO_3$ pPv will dissociate into CsCl-type MgO and $MgSi_2O_5$ ($P2_1/c$-type) at 900 GPa (Umemoto and Wentzcovitch, 2011; **Figures 13** and **17**). The volume change associated with this transition is ~2%, and the Si^{4+} coordination increases from 6 in postperovskite to 7–8 in $MgSi_2O_5$. A further dissociation of $MgSi_2O_5$ into MgO and SiO_2 (Fe_2P phase, ninefold coordination) is also predicted to occur with a small volume change at 2.1 TPa, a pressure above the maximum expected to occur in super-Earth mantles (Umemoto and Wentzcovitch, 2011). Quasiharmonic calculations suggest both dissociation reactions are endothermic with negative Clapeyron slopes, thereby yielding a wider stability field for the dissociation products at higher temperatures. The negative Clapeyron slope arises due to changes in the vibrational density of states resulting from increasing Si–O bond lengths as Si^{4+} coordination increases across each transition.

2.07.5.2.5 $CaSiO_3$ and CaO

$CaSiO_3$ perovskite is the third most abundant phase in Earth's mantle. Theoretical calculations find that at 0 K, $CaSiO_3$ perovskite transforms to postperovskite above 500 GPa and then dissociates to CaO (B2 phase) and SiO_2 (Fe_2P phase) around 700 GPa (Tsuchiya and Tsuchiya, 2011). However, at the higher temperatures expected in exoplanets, quasiharmonic calculations indicate that the postperovskite phase is not stable and $CaSiO_3$ perovskite directly decomposes to CaO (B2) and SiO_2 (pyrite type) at 600 GPa (Tsuchiya and Tsuchiya, 2011; **Figure 13**). The breakdown of $CaSiO_3$ occurs at considerably lower pressure than the stability limit of $MgSiO_3$ (~900 GPa). SiO_2 liberated by the breakdown of $CaSiO_3$ would react with MgO to increase the total abundance of the postperovskite phase (Tsuchiya and Tsuchiya, 2011). The oxide CaO transforms to the B2 phase at low pressures of ~60 GPa (Jeanloz et al., 1979; Mehl et al., 1988; (**Figure 13**). The B2 phase of CaO is predicted theoretically to metallize at ~400 GPa, but other oxides (SiO_2 and MgO) remain insulating to 2000 GPa at low temperatures (Oganov et al., 2003; Tsuchiya and Tsuchiya, 2011).

2.07.5.2.6 Al_2O_3

Al_2O_3 crystallizes in the corundum structure at ambient conditions and undergoes transformations to the Rh_2O_3-II structure at ~90 GPa and the $CaIrO_3$ structure at ~130 GPa (Cynn et al., 1990; Funamori and Jeanloz, 1997; Marton and Cohen, 1994; Oganov and Ono, 2005; **Figure 13**). Metallization of Al_2O_3 may occur at pressures of ~300 GPa (Nellis, 2010). DFT calculations predict further structural transformation at

370 GPa to a U_2S_3-type phase (Umemoto and Wentzcovitch, 2008). For the Earth, the Al_2O_3 component of the mantle is largely dissolved into the (Mg,Fe)SiO_3 perovskite, post-perovskite, or other Al-rich phases and free Al_2O_3 is not expected. The change in cation coordination from six to seven in the U_2S_3 phase may favor exsolution of Al_2O_3 out of the postperovskite phase in deep super-Earths with possible resulting changes in electrical and thermal conductivities for the assemblage (Umemoto and Wentzcovitch, 2008).

2.07.5.2.7 Iron and iron alloys

Under pressure, iron transforms from the body-centered-cubic (bcc, α) phase to a hexagonal-close-packed (hcp, ε) phase near 13 GPa. Most experiments suggest that the hcp phase remains stable to higher pressures up to those of Earth's core (Kuwayama et al., 2008; Ma et al., 2004; Shen et al., 1998; Tateno et al., 2010), although some experimental evidence for new phases has been reported (Andrault et al., 1997; Dubrovinsky et al., 2000). Theoretical calculations report conflicting results with some studies favoring the stability of hcp iron at Earth core conditions (Modak et al., 2007; Vočadlo et al., 1999), while various other possible phases have been also proposed including bcc (Belonoshko et al., 2011; Bouchet et al., 2013; Luo et al., 2010), face-centered-cubic (fcc) (Mikhaylushkin et al., 2009), or stacking disordered phases (Cottenier et al., 2011; Ishikawa et al., 2011). Recently, static DAC experiments have reached inner core conditions up to 377 GPa and 5700 K (Tateno et al., 2010) and found that the hcp phase of Fe is stable. However, further studies at these extreme conditions are needed for confirmation.

The EOS of iron has been studied under quasihydrostatic conditions in the DAC up to 300 GPa (Dewaele et al., 2006; Dubrovinsky et al., 2000). Extensive shock compression data sets have been obtained on iron, and a careful analysis of data to 442 GPa has been reported (Brown et al., 2000) Under shock loading, iron is observed to melt along the Hugoniot at about 230 GPa (Brown and McQueen, 1986; Nguyen and Holmes, 2004). Laser-based ramp compression experiments have constrained the quasi-isentropic compression curve of solid iron to 273 GPa (Wang et al., 2013).

Theoretical DFT studies have examined the stable phases and structure of iron to pressures as high as 100 TPa (Cottenier et al., 2011; Pickard and Needs, 2009; Stixrude, 2012). The hcp phase is found to be stable at 0 K to pressures of and well beyond those of Earth's core. A transformation to an fcc phase occurs at 6–7 TPa with a volume change of ~0.15%. At even higher pressures, a body-centered-tetragonal phase is stabilized at 34–38 TPa. Ab initio random structure searching showed that only these high-symmetry close-packed phases are energetically competitive candidates for iron (Pickard and Needs, 2009). Results at finite temperatures on these close-packed phases have been reported using the QHA and are consistent with the 0 K results (Stixrude, 2012; **Figure 18**). The central pressure for a large (10 M_E) super-Earth is expected to be around 4 TPa (Wagner et al., 2012) and that of Jupiter (~300 M_E) is around 7 TPa. Thus, hcp iron is likely the stable phase under conditions of all or nearly all super-Earths, but the high-pressure phases of iron would be expected to exist in the cores of super-Jupiters. However, other recent theoretical studies suggest that bcc iron or more complex structures composed

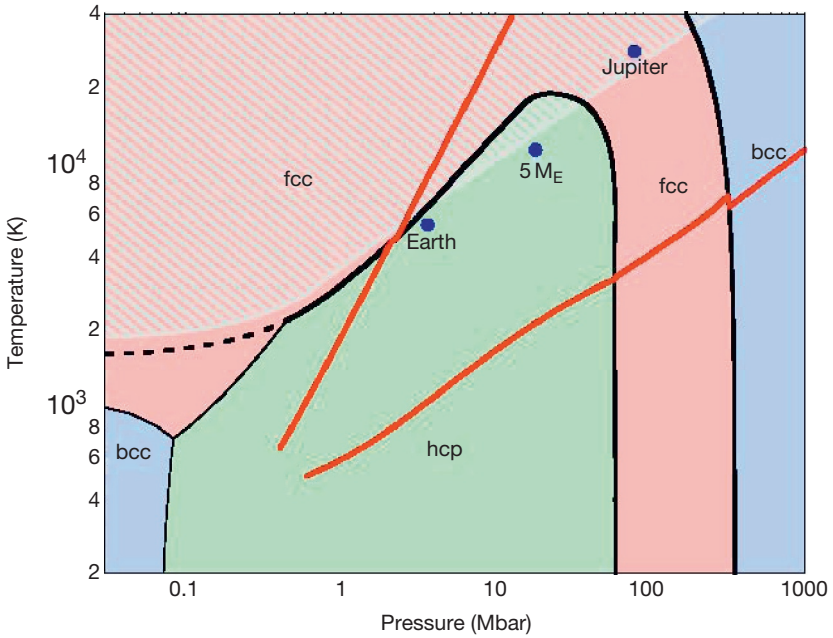

Figure 18 Phase diagram of Fe at ultrahigh pressures. Thin black lines show experimental phase boundaries; thick black lines are from theoretical calculations. The red lines show calculated isentrope (lower) and Hugoniot curves (upper). *P–T* conditions at the center of the Earth, a super-Earth with mass five times the Earth's mass, and Jupiter are shown by the blue circles. The stability field of liquid iron, indicated by the hatching, is estimated from computed vibrational frequencies and Lindemann's law. bcc, body-centered-cubic phase; fcc, face-centered-cubic phase; hcp, hexagonal-close-packed phase. Reproduced from Stixrude L (2012) Structure of iron to 1 Gbar and 40 000 K. *Physical Review Letters* 108(5): 055505. http://dx.doi.org/10.1103/PhysRevLett.108.055505, with permission.

of periodic stacking fault sequences are candidate structures for exoplanet cores (Bouchet et al., 2013; Cottenier et al., 2011). The stable phase of iron may also be affected by impurity content (Dubrovinsky et al., 2007). There have been extensive experimental and theoretical studies of various iron alloys that are candidate Earth core components (**Chapter 2.06**), but few constraints exist as yet at *P*–*T* conditions relevant to super-Earths.

Using ab initio MD simulations, the melting curve of iron has been computed to pressures up to 1500 GPa (Bouchet et al., 2013; Morard et al., 2011). The results are in good agreement with earlier calculations extending up to pressures of the Earth's inner core. By comparing to *P*–*T* conditions expected in super-Earths from interior models (Sotin et al., 2007; Valencia et al., 2006; Wagner et al., 2012), it was found that Clapeyron slope of the melting curve exceeded the geotherm for super-Earths and the likelihood of a molten core decreases as the size of a terrestrial planet increases (Morard et al., 2011). Recent thermal evolution models suggest that an inner core will not develop for super-Earths greater than 2.5 M_E (Gaidos et al., 2010). However, the role of melting point depression of iron due to alloying components remains to be evaluated. There is also a need for more studies on the key physical properties of iron and iron alloys necessary for understanding core energetics and dynamics for super-Earths. A number of thermodynamic properties (thermal expansivity, Grüneisen parameter, etc.) of iron have been evaluated up to 1500 GPa and high T using ab initio MD computations (Bouchet et al., 2013).

2.07.5.2.8 Diamond and carbides

Carbon-rich planets may result from C enrichment of a local area of the protoplanetary disk or due to variation in host star chemical abundance (Bond et al., 2010). Carbon is the fourth most abundant element in the cosmos and a key constituent of many planets. Ice giants such as Neptune and Uranus contain large quantities of methane (Hubbard et al., 1991) that decomposes under high-pressure and high-temperature conditions, possibly forming diamond-rich layers in the interior (Ancilotto et al., 1997; Benedetti et al., 1999; Ross, 1981). Static DAC experiments have constrained the EOS of diamond to 140 GPa (Occelli et al., 2003), while maximum static pressures of up to 400 GPa have been reached on diamond samples (Akahama and Kawamura, 2010; Wang et al., 2010). Using laser-based ramp compression, the pressure–density relationship and strength of diamond have been characterized up to 800 GPa (Bradley et al., 2009).

Theoretical calculations predict that diamond will transform to the BC8 structure at around 1 TPa followed by a further transition to a simple-cubic structure near 3 TPa (Correa et al., 2008; Grumbach and Martin, 1996; Yin, 1984; Yin and Cohen, 1983; **Figure 19**). The BC8 phase remains tetrahedrally coordinated and strongly covalently bonded but is about 10% denser than diamond due to denser packing of tetrahedra. It is also predicted to be weakly metallic. The transition to the simple-cubic structure results in an increase in coordination number to six. Experimental evidence for the existence of a new solid phase, possibly BC8, in shock-compressed diamond, has been reported at around 850–900 GPa (Knudson et al., 2008). Ab initio random structure search methods have been used to predict a further sequence of transformations from simple-cubic, to simple-hexagonal (6.4 TPa), to fcc (21 TPa), to double hcp (270 TPa), to bcc (650 TPa) phase (Martinez-Canales et al., 2012). The fcc phase of carbon has the interesting property that it is an electride in which electrons play the role of anions in the structure.

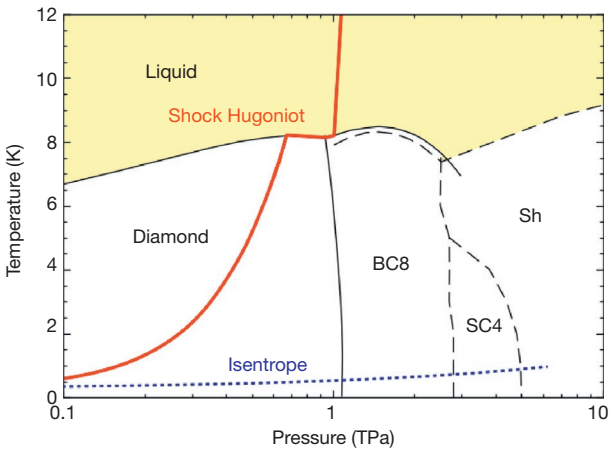

Figure 19 Phase diagram of carbon at ultrahigh pressures. Isentrope is shown as blue dotted line, and shock Hugoniot is solid red line. The yellow region is liquid carbon. SC4, simple-cubic phase; Sh, simple-hexagonal phase. Reproduced from Rygg JR, et al. (2012) Powder diffraction from solids in the terapascal regime. *Review of Scientific Instruments* 83(11): 113904. http://dx.doi.org/10.1063/1.4766464, with permission.

The melting behavior of diamond has also attracted much interest (**Figure 19**). Theoretical studies have predicted a maximum in the melting curve around 500 GPa and 8000–9000 K (Correa et al., 2006; Grumbach and Martin, 1996; Wang et al., 2005; Wu et al., 2002). Also, a triple point between diamond, the BC8 phase, and liquid is predicted to exist at ~850 GPa from ab initio MD simulations (Correa et al., 2006). Shock compression experiments on diamond have been carried out to as high as 4 TPa (Bradley et al., 2004; Brygoo et al., 2007; Eggert et al., 2009; Hicks et al., 2008; Knudson et al., 2008; Nagao et al., 2006). These studies reveal that at 600–1100 GPa, diamond melts to a dense metallic fluid with a negative melting slope consistent with the theoretical predictions.

SiC is a potential major phase in carbon-rich planets. Its behavior has been explored under both static and shock compressions to as high as 160 GPa. At ~100 GPa, SiC undergoes a transition from the wurtzite to rock-salt structure with a large (~15%) density increase (Sekine and Kobayashi, 1997; Yoshida et al., 1993). Due to such a large density change, this transformation could be a major structural feature in carbide-rich exoplanets. EOS data for the high-pressure phase of SiC are not available, and so models to date have used EOS parameters for the low-pressure phase (Madhusudhan et al., 2012; Seager et al., 2007). The thermal structure of a carbide-rich planet may be drastically different from planets with silicate-/oxide-dominated mantles due to large variations in physical properties. For example, the thermal conductivity of SiC is two orders of magnitude greater than that of silicates and oxides, likely implying major differences in thermal structure and evolution (Madhusudhan et al., 2012). Additionally, SiC has been found

to have a negative Clapeyron slope for melting, at least up to modest pressures (~8 GPa) (Sokolov et al., 2012), and may result in a solid SiC layer underlain by a molten SiC layer, provided that the densities remain high for the melt.

2.07.5.2.9 H_2O

In addition to planets with largely dry and rocky compositions, super-Earths may also encompass a significant amount of water along with refractory components (ocean planets) (Léger et al., 2004) or may be dominantly composed of ices with a H_2–He envelope (sub-Neptunes). Such planets might form outside the snow line of the protoplanetary disk allowing them to accrete and retain significant quantities of ice and, in some circumstances, could subsequently migrate inward. The ability to retain H_2–He and H_2O over the planet's evolution will depend on a number of factors including its final distance from the host star. H_2O ice is a complex material with 16 stable or metastable crystalline phases identified experimentally (Figure 20). At temperatures above 150 K, ice VI occurs approximately from 0.6 GPa until it transforms to ice VII at 2.2 GPa. Ice VII is stable to ~70 GPa where it transforms to ice X. In this phase, the structure adopts a symmetric configuration in which oxygen atoms form a bcc lattice and the hydrogen atoms are located at the midpoints between two nearest-neighbor oxygen atoms. A further transformation from ice X to a new phase (ice XI) is predicted to occur at ~3 Mbar and to remain stable up to at least ~2000 K and 4 Mbar, based on ab initio MD simulations (Benoit et al., 1996). Higher-pressure phase transitions have been explored using DFT-based structure searching methods (Hermann et al., 2012; Ji et al., 2011; Militzer and Wilson, 2010).

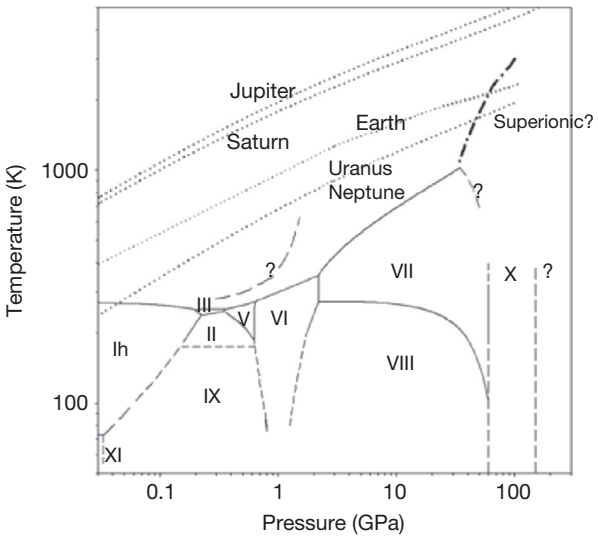

Figure 20 High-pressure–temperature phase diagram of H_2O. The Roman numerals are various phases of solid ices. Ih represents ice in the hexagonal crystal structure stable at ambient conditions. Black solid lines show experimentally determined phase boundaries; dashed lines show schematic phase boundaries; dotted lines show isentropes of Jupiter, Saturn, Uranus, and Neptune, respectively, and geotherm of the Earth. The dashed line in the liquid region is a proposed liquid–liquid transition. Reproduced from Lin et al. (2005) Melting behavior of H_2O at high pressures and temperatures. *Geophysical Research Letters* 32: L11306, with permission.

Assuming full differentiation, a rocky planet with a substantial H_2O/ice component would feature H_2O layer(s) overlying the rocky mantle and metallic core. Depending on surface P–T conditions, H_2O at the surface of such a planet could be solid or liquid, possible forming a liquid ocean to depths of ~100 km (Léger et al., 2004). Because the slope of adiabatic temperature gradient in the liquid H_2O layer is lower than the slope of the melting curve of high-pressure ice phases, the water layer would eventually freeze into ice VI or ice VII. Ice VII eventually transforms at ~70 GPa to ice X, which is stable to at least 150 GPa. For a planet that is 50 wt% H_2O, the P–T conditions at the base of the ice layer are estimated to be ~50 GPa and <1000 K (Sotin et al., 2007) for a 1 M_E planet. The thickness of the ice layer would range from 3000 to 6000 km for planets ranging from 1 to 10 M_E (Sotin et al., 2007).

2.07.6 Physical Properties of Minerals at Super-Earth Conditions

Mineralogical phase transitions change the density structure of a planet, although the effect on the mass–radius relationship is not expected to be large in many cases (Swift et al., 2012). Changes in crystal structure, however, can affect other key properties including melting temperature, thermal expansivity, Grüneisen parameter, thermal and electrical conductivities, and rheological properties, which are all critical for understanding the structure, dynamics, and evolution of exoplanets. Because of the wider range of pressures and temperatures encountered in super-Earth interiors, the depth dependence of thermodynamic, rheological, and transport properties may become especially important.

2.07.6.1 Rheology

The thermal structure, convective regime, tectonic and magmatic activity, propensity for plate tectonics, and existence of a magnetic field are all properties strongly influenced by the viscosity structure of a planet. The viscosity is determined by the rheological properties of the constituent minerals. Under the high-temperature, low-stress conditions expected in terrestrial planetary mantles, viscous deformation of solids is controlled by thermally activated motion of crystalline defects (Karato, 2008; Poirier, 1985). The pressure and temperature dependence of the viscosity, η, can be described in a simplified Arrhenius-type formulation (Karato, 2011; Wagner et al., 2012):

$$\eta(P,T) = b\exp\left(\frac{E^* + PV^*(P)}{RT}\right) \qquad [17]$$

where b is a constant, R is the gas constant, E^* is the activation energy, and V^* is the activation volume. Viscosity is both strongly pressure- and temperature-dependent with the activation energy controlling the temperature effect of viscosity and the activation volume controlling the pressure effect.

In the Earth, viscosity increases with pressure due to reduction of the activation volume for creep. The viscosity of the deep lower mantle is estimated to be 10–100 times

higher than Earth's upper mantle (see Chapter 7.02). However, direct experimental measurements of the effect of pressure on activation volume are limited and uncertain. One approach to estimate the effect of pressure on viscosity for conditions relevant to a 10 M_E planet is by scaling with the homologous temperature, T/T_m, where T_m is the melting temperature (Stamenkovic et al., 2011). The melting temperature of perovskite, taken to be representative of exoplanet mineralogy, was inferred from Lindemann's law, which assumes that melting occurs when the root-mean-square atomic displacements reach a critical fraction of the interatomic spacing. Using this approach, the mantle viscosity was predicted to increase greatly by up to 15 orders of magnitude across the adiabatic mantle of a 10 M_E planet (Stamenkovic et al., 2011). The viscosity at the bottom of the mantle in this case would be sufficiently large that a conductive lid would form above the core–mantle boundary with major effects on the thermal structure and evolution of the planet (Stamenkovic et al., 2012).

Vacancy diffusion rates in $MgSiO_3$ perovskite and postperovskite at lower mantle conditions have been calculated using first-principles methods and transition state theory (Ammann et al., 2010). The predicted viscosity of the two phases inferred from the diffusion-controlled creep strength is different with viscosities in postperovskite up to four orders of magnitude lower than perovskite. Postperovskite also exhibits highly anisotropic behavior with several orders of magnitude difference in activation energy in different directions. These results for postperovskite have subsequently been extended to pressures up to 1 TPa, leading to a prediction of viscosities ($\sim 10^{25}$–10^{26} Pa s) in the deep mantle of a large super-Earth (7–10 M_E). These are only 4–5 orders of magnitude greater than those in the Earth's lower mantle. Corresponding numerical convection calculations find that convection can still occur in the deep mantle of such a planet due to feedbacks between internal heating, temperature, and viscosity (Tackley et al., 2013). However, it has also been argued that the theoretical calculations on defect mobility in postperovskite are not sufficient to constrain creep behavior of this mineral (Karato, 2010).

Other recent work, on the other hand, suggests that the solid viscosity in large exoplanet mantles may be relatively low at depth (Karato, 2011). Pressure weakening is predicted to occur due to several factors. One is the expected change in the mechanism of diffusion from vacancy to interstitial-dominated beginning at ~100 GPa. In general, oxides are weaker than silicates and B2 oxides are weaker than B1 oxides (Karato, 1989). As such, dissociation of $CaSiO_3$ and $MgSiO_3$ forming B2-type MgO and CaO at 600–1100 GPa will increase the volume fraction of these relatively weak oxides. If metallization of the oxides occurs at high P–T, it may lead to further weakening. As a result of these factors, the deep mantle viscosity of terrestrial super-Earths may decrease as planetary mass increases. The deep mantle of a large rocky super-Earth may have viscosities that are 100–1000 times lower than those of Earth's lower mantle (Karato, 2011). Whether MgO and CaO would be sufficiently abundant to control the rheological properties of the mixture will ultimately depend on the bulk composition of the planet's mantle and whether complete (Umemoto et al., 2006a) or partial dissociation (Umemoto and Wentzcovitch, 2011) of $MgSiO_3$ occurs. Clearly, in view of the large differences of the previously mentioned studies, there remains substantial uncertainty about the rheological behavior at these extreme conditions, as there are many orders of magnitude differences in viscosity estimates in super-Earth interiors.

In addition to their potential effect on rheology, phase transitions can promote layered convection when accompanied by a strong negative Clapeyron slope that resists convection (Tackley et al., 1993; van den Berg et al., 2010). Temperatures in super-Earth interiors are highly uncertain as discussed in previous sections. The temperature has a strong effect on rheology, and there is a feedback between temperature and rheology that regulates the heat loss of a planet and influences its thermal evolution. The proximity of many candidate super-Earths to their host star means that they are expected to be in synchronous rotation and subjected to strong tidal forces. The amount and distribution of tidal heating will depend on the viscosity, shear modulus, and density (Moore, 2003). Tidal friction can contribute substantially to the total heat budget of short-period super-Earths (Henning et al., 2009). Orbital evolution of exoplanets is also an important phenomenon. Lower viscosities would favor higher tidal heating rates and therefore faster orbital evolution.

2.07.6.2 Thermal Expansivity and Thermal Conductivity

Thermal expansivity, α, determines the buoyancy in the deep mantle and hence influences convective motion in planets. Thermodynamic calculations for mantle phases yield estimates of approximately an order of magnitude decrease in thermal expansivity from ambient pressure up to ~1 TPa along a plausible super-Earth temperature profile (Stamenkovic et al., 2011; Wagner et al., 2012). This is much greater than the ~2.5 times decrease in α expected across the Earth's mantle, and this strong decrease may affect the style and vigor of convection in super-Earth deep mantles. There are as yet few experimental measurements or theoretical calculations of thermal expansivity in the multimegabar range relevant to super-Earth interiors.

Thermal conductivities of mantle phases are also important parameters for thermal models. The thermal conductivity controls the temperature gradient across boundary layers that transfer heat conductively. However, this property is not well constrained for mantle minerals due to difficulties in both theoretical calculations and experiments at high pressures and temperatures. Thermal conductivity is the sum of a phonon or lattice component, a radiative component, and an electronic component. The phonon contribution is expected to be dominant under high-pressure interior conditions. In general, the phonon contribution to thermal conductivity increases with pressure, and this would tend to reduce convective vigor as planetary size increases (Wagner et al., 2012). At the high temperatures of exoplanet interiors, the electronic component of thermal conductivity may play an increasingly strong role (van den Berg et al., 2010). Experimental studies suggest that the thermal conductivity and diffusivity of postperovskite may be significantly larger than that of perovskite (Hunt et al., 2012; Ohta et al., 2012b). Dissociation of silicates into oxides could affect deep mantle thermal

conductivities with expected higher conductivity in oxides (de Koker, 2010). For the largest super-Earths, metallization of mantle phases (discussed in the succeeding text) would also enhance electronic conductivities while suppressing radiative conductivity (Umemoto et al., 2006a). The potential effects of such factors on heat transport and convective dynamics in super-Earths have been explored in a number of recent works (Stamenkovic et al., 2011; Tosi et al., 2010; van den Berg et al., 2010; Wagner et al., 2012).

2.07.6.3 Electrical Conductivity and Metallization

Pressure reduces interatomic distances causing electron wave functions of neighboring ions to increasingly overlap. Eventually, outer electrons become delocalized resulting in increased electrical conductivity and ultimately metallization. Experimental and theoretical evidence for high-pressure metallization of potential super-Earth mantle phases such as FeO, MgO, Al_2O_3, SiO_2, and CaO was discussed earlier. Metallization may affect rheology and thermal and radiative heat transport. Additionally, electrically conducting phases in the deep lower mantle could potentially interact with the magnetic field generated by a core dynamo affecting possible direct or indirect observations of super-Earth magnetic fields such as by radio emission, x-ray emission from planet-hosting stars, or exoplanet atmospheric effects. Numerical dynamo models examining how metallized silicates in the deep mantles may affect the observable magnetic fields of super-Earths indicate that such metallization would reduce the detectability of dynamo-generated magnetic fields (Vilim et al., 2013). The presence of deep magma oceans in terrestrial exoplanets could lead to metallic silicate/oxide liquid regions or layers that could contribute to dynamo processes in a planet (McWilliams et al., 2012; Nellis, 2012).

2.07.6.4 Melts and Liquids

An understanding of melting behavior and the properties of liquid silicates and metal alloys at ultrahigh P–T conditions are also needed for super-Earth applications. Heating during accretion and differentiation in the early stages of planetary evolution is likely sufficient to melt the silicate mantle of terrestrial planets, creating magma oceans that could span a wide range of depths. Degassing of such oceans may play a major role in the development of early atmospheres and affect volatile retention in the interior. Extreme temperatures in close-in tidally locked planets with permanent day- and nightsides could result in localized lava oceans beneath the substellar point or allow enhanced magma production in the substellar hemisphere of the planet (Gelman et al., 2011; Léger et al., 2011). High internal temperatures leading to partial melting may also occur as a result of compositional layering, rheological properties, or tidal forcing. In such cases, a deep magma ocean such as proposed for Earth (Labrosse et al., 2007) may develop in terrestrial exoplanets (Tackley et al., 2013; Valencia et al., 2007b). While some constraints on melting curves and liquid properties from theory and experiment are available for some of the materials as discussed earlier, there is still considerable uncertainty in many fundamental properties including solidus temperature, melt–solid density contrast, and partitioning behavior at the pressures of 100–1000 GPa and beyond.

2.07.7 Summary and Outlook

Less than two decades after the discovery of the first confirmed extrasolar planet, there are at the time of this writing more than 900 confirmed and over 3000 additional candidate exoplanets. As techniques for detecting and probing exoplanets extend to smaller bodies more distant from their host stars, there is growing interest in understanding the prevalence and characteristics of the emerging population of super-Earth planets. Such bodies may encompass a diverse range of composition and behavior for which there may be in many cases no analog in our own solar system. Speculations about planetary types that exist include Earth-like compositions, super-Mercuries, coreless planets, core-only planets, water worlds, carbon-rich planets, and sub-Neptunes.

Inferring the mineralogy and internal structure of exoplanets is very challenging given the limited observational constraints possible, but these properties are of key importance for understanding the diversity of planetary worlds. For solid exoplanets, the interior structure is intrinsically interlinked to interpretation of observations and to models of planet formation and atmospheric processes. The interior structure not only controls the thermal evolution of the interior but also exerts a strong influence on the surface environment including the nature of the atmosphere, existence of a magnetic field, and tectonic style. The interior behavior is thus a critical ingredient for determining whether surface conditions are conducive to habitability. Ultimately, the large-scale interior processes of planets are controlled by the physical properties of the mineral constituents, which in turn are controlled by their underlying chemistry and crystal structure. Unraveling the range of structures and chemistries for the range of plausible constituents of super-Earths represents an exciting challenge for mineralogy and mineral physics in the coming years. Addressing this problem will require development of new experimental techniques to reach even higher pressures and temperatures concurrent with further advances in first-principles theoretical methods. The field of exoplanet mineralogy is in its infancy, but results to date are already leading to novel findings and substantial revisions in our understanding of how solid materials behave at extreme conditions. This chapter represents a snapshot in our understanding at this early juncture. The rapid pace of development in observation, experiment, and interpretation promises many new and exciting discoveries in the coming years.

Acknowledgments

This work was supported by the NSF and NNSA. NM acknowledges support from the Yale Center for Astronomy and Astrophysics (YCAA) through the YCAA Fellowship. Jue Wang (Princeton) provided assistance with some figures.

References

Ahrens TJ (1987) Shock wave techniques for geophysics and planetary physics. In: Sammis CG and Henyey TL (eds.) *Methods of Experimental Physics*, pp. 185–235. New York: Academic.

Akahama Y and Kawamura H (2010) Pressure calibration of diamond anvil Raman gauge to 410 GPa. *Journal of Physics: Conference Series* 215: 012195. http://dx.doi.org/10.1088/1742-6596/215/1/012195.

Akins JA and Ahrens TJ (2002) Dynamic compression of SiO_2: A new interpretation. *Geophysical Research Letters* 29(10): 1394. http://dx.doi.org/10.1029/2002GL014806.

Alfe D (2005) Melting curve of MgO from first-principles simulations. *Physical Review Letters* 94(23): 235701. http://dx.doi.org/10.1103/PhysRevLett.94.235701.

Alfe D, Alfredsson M, Brodholt J, Gillan M, Towler M, and Needs R (2005) Quantum Monte Carlo calculations of the structural properties and the B1–B2 phase transition of MgO. *Physical Review B* 72(1): 014114. http://dx.doi.org/10.1103/PhysRevB.72.014114.

Ammann MW, Brodholt JP, Wookey J, and Dobson DP (2010) First-principles constraints on diffusion in lower-mantle minerals and a weak D″ layer. *Nature* 465(7297): 462–465. http://dx.doi.org/10.1038/nature09052.

Ancilotto F, Chiarotti GL, Scandolo S, and Tosatti E (1997) Dissociation of methane into hydrocarbons at extreme (planetary) pressure and temperature. *Science* 275(5304): 1288–1290. http://dx.doi.org/10.1126/science.275.5304.1288.

Andrault D, Fiquet G, Kunz M, Visocekas F, and Häusermann D (1997) The orthorhombic structure of iron: An in situ study at high temperature and high pressure. *Science* 278(5339): 831–834. http://dx.doi.org/10.1126/science.278.5339.831.

Asplund M, Grevesse N, Sauval AJ, and Scott P (2009) The chemical composition of the Sun. In: Blandford R, Kormendy J, and VanDishoeck E (eds.) *Annual Review of Astronomy and Astrophysics*, vol. 47, pp. 481–522. Palo Alto, CA: Annual Reviews.

Badro J, Rueff JP, Vanko G, Monaco G, Fiquet G, and Guyot F (2004) Electronic transitions in perovskite: Possible nonconvecting layers in the lower mantle. *Science* 305(5682): 383–386. http://dx.doi.org/10.1126/science.1098840.

Baraffe I, Chabrier G, and Barman T (2008) Structure and evolution of super-Earth to super-Jupiter exoplanets I. Heavy element enrichment in the interior. *Astronomy and Astrophysics* 482(1): 315–332. http://dx.doi.org/10.1051/0004-6361:20079321.

Batalha NM, et al. (2011) Kepler's first rocky planet: Kepler-10b. *Astrophysical Journal* 729(1): 27. http://dx.doi.org/10.1088/0004-637X/729/1/27.

Batalha NM, et al. (2013) Planetary candidates observed by Kepler. iii. Analysis of the first 16 months of data. *Astrophysical Journal Supplement Series* 204(2): 24.

Bean JL, Kempton EM-R, and Homeier D (2010) A ground-based transmission spectrum of the super-Earth exoplanet GJ 1214b. *Nature* 468(7324): 669–672. http://dx.doi.org/10.1038/nature09596.

Belonoshko A, Arapan S, Martonak R, and Rosengren A (2010) MgO phase diagram from first principles in a wide pressure–temperature range. *Physical Review B* 81(5): 054110. http://dx.doi.org/10.1103/PhysRevB.81.054110.

Belonoshko AB, Arapan S, and Rosengren A (2011) An ab initio molecular dynamics study of iron phases at high pressure and temperature. *Journal of Physics: Condensed Matter* 23(48): 485402. http://dx.doi.org/10.1088/0953-8984/23/48/485402.

Benedetti LR, Nguyen JH, Caldwell WA, Liu HJ, Kruger M, and Jeanloz R (1999) Dissociation of CH_4 at high pressures and temperatures: Diamond formation in giant planet interiors? *Science* 286(5437): 100–102. http://dx.doi.org/10.1126/science.286.5437.100.

Benoit M, Bernasconi M, Focher P, and Parrinello M (1996) New high-pressure phase of ice. *Physical Review Letters* 76(16): 2934–2936. http://dx.doi.org/10.1103/PhysRevLett.76.2934.

Birch F (1952) Elasticity and constitution of the Earth interior. *Journal of Geophysical Research* 57(2): 227–286. http://dx.doi.org/10.1029/JZ057i002p00227.

Boates B and Bonev SA (2013) Demixing instability in dense molten $MgSiO_3$ and the phase diagram of MgO. *Physical Review Letters* 110(13): 135504. http://dx.doi.org/10.1103/PhysRevLett.110.135504.

Boehly TR, et al. (1997) Initial performance results of the OMEGA laser system. *Optic Communication* 133(1–6): 495–506. http://dx.doi.org/10.1016/S0030-4018(96)00325-2.

Bond JC, O'Brien DP, and Lauretta DS (2010) The compositional diversity of extrasolar terrestrial planets. I. In situ simulations. *Astrophysical Journal* 715(2): 1050–1070. http://dx.doi.org/10.1088/0004-637X/715/2/1050.

Borucki WJ, et al. (2010) Kepler planet-detection mission: Introduction and first results. *Science* 327(5968): 977–980. http://dx.doi.org/10.1126/science.1185402.

Boslough MB and Asay JR (1993) Basic principles of shock compression. In: Asay JR and Shahinpoor M (eds.) *High-Pressure Shock Compression of Solids*, pp. 7–42. New York: Springer.

Bouchet J, Mazevet S, Morard G, Guyot F, and Musella R (2013) Ab initio equation of state of iron up to 1500 GPa. *Physical Review B* 87(9): 094102. http://dx.doi.org/10.1103/PhysRevB.87.094102.

Bradley DK, Eggert JH, Hicks DG, et al. (2004) Shock compressing diamond to a conducting fluid. *Physical Review Letters* 93(19): 195506. http://dx.doi.org/10.1103/PhysRevLett.93.195506.

Bradley DK, Eggert JH, Smith RF, et al. (2009) Diamond at 800 GPa. *Physical Review Letters* 102(7): 075503. http://dx.doi.org/10.1103/PhysRevLett.102.075503.

Brown JM, Fritz JN, and Hixson RS (2000) Hugoniot data for iron. *Journal of Applied Physics* 88(9): 5496–5498. http://dx.doi.org/10.1063/1.1319320.

Brown JM and McQueen RG (1986) Phase transitions, Gruneisen parameter and elasticity for shocked iron between 77 GPa and 400 GPa. *Journal of Geophysical Research* 91(B7): 7485–7494.

Bruntt H, Deleuil M, Fridlund M, et al. (2010) Improved stellar parameters of CoRoT-7: A star hosting two super Earths. *Astronomy and Astrophysics* 519: A51. http://dx.doi.org/10.1051/0004-6361/201014143.

Brygoo S, Henry E, Loubeyre P, et al. (2007) Laser-shock compression of diamond and evidence of a negative-slope melting curve. *Nature Materials* 6(4): 274–277. http://dx.doi.org/10.1038/nmat1863.

Buchhave LA, et al. (2012) An abundance of small exoplanets around stars with a wide range of metallicities. *Nature* 486(7403): 375–377. http://dx.doi.org/10.1038/nature11121.

Carter-Bond JC, O'Brien DP, Delgado Mena E, Israelian G, Santos NC, and Gonzalez Hernandez JI (2012a) Low Mg/Si planetary host stars and their Mg-depleted terrestrial planets. *Astrophysical Journal Letters* 747(1): L2. http://dx.doi.org/10.1088/2041-8205/747/1/L2.

Carter-Bond JC, O'Brien DP, and Raymond SN (2012b) The compositional diversity of extrasolar terrestrial planets II. Migration simulations. *Astrophysical Journal* 760(1): 44. http://dx.doi.org/10.1088/0004-637X/760/1/44.

Ceperley DM (2010) An overview of quantum Monte Carlo methods. *Reviews in Mineralogy and Geochemistry* 71: 129–135.

Charbonneau D, et al. (2009) A super-Earth transiting a nearby low-mass star. *Nature* 462(7275): 891–894. http://dx.doi.org/10.1038/nature08679.

Cohen RE, Gulseren O, and Hemley RJ (2000) Accuracy of equation-of-state formulations. *American Mineralogist* 85(2): 338–344.

Coppari F, Smith RF, Eggert JH, et al. (2013) X-ray diffraction study of a new phase of MgO at exo-planet interior pressures. *Nature Geoscience* 6: 926–929.

Correa AA, Benedict LX, Young DA, Schwegler E, and Bonev SA (2008) First-principles multiphase equation of state of carbon under extreme conditions. *Physical Review B* 78(2): 024101. http://dx.doi.org/10.1103/PhysRevB.78.024101.

Correa AA, Bonev SA, and Galli G (2006) Carbon under extreme conditions: Phase boundaries and electronic properties from first-principles theory. *Proceedings of the National Academy of Sciences of the United States of America* 103(5): 1204–1208. http://dx.doi.org/10.1073/pnas.0510489103.

Cottenier S, Probert MIJ, Van Hoolst T, Van Speybroeck V, and Waroquier M (2011) Crystal structure prediction for iron as inner core material in heavy terrestrial planets. *Earth and Planetary Science Letters* 312(1–2): 237–242. http://dx.doi.org/10.1016/j.epsl.2011.09.045.

Cynn H, Isaak D, Cohen R, Nicol M, and Anderson O (1990) A high-pressure phase-transition of corundum predicted by the potential induced breathing model. *American Mineralogist* 75(3–4): 439–442.

Danson CN, et al. (1998) Well characterized 1019 W/cm^2 operation of VULCAN: An ultra-high power Nd: Glass laser. *Journal of Modern Optics* 45(8): 1653–1669. http://dx.doi.org/10.1080/09500349808230660.

De Koker N (2010) Thermal conductivity of MgO periclase at high pressure: Implications for the D″ region. *Earth and Planetary Science Letters* 292(3–4): 392–398. http://dx.doi.org/10.1016/j.epsl.2010.02.011.

De Koker N and Stixrude L (2009) Self-consistent thermodynamic description of silicate liquids, with application to shock melting of MgO periclase and $MgSiO_3$ perovskite. *Geophysical Journal International* 178(1): 162–179. http://dx.doi.org/10.1111/j.1365-246X.2009.04142.x.

Dekura H, Tsuchiya T, Kuwayama Y, and Tsuchiya J (2011a) Theoretical and experimental evidence for a new post-cotunnite phase of titanium dioxide with significant optical absorption. *Physical Review Letters* 107(4): 045701. http://dx.doi.org/10.1103/PhysRevLett.107.045701.

Dekura H, Tsuchiya T, and Tsuchiya J (2011b) First-principles prediction of post-pyrite phase transitions in germanium dioxide. *Physical Review B* 83(13): 134114. http://dx.doi.org/10.1103/PhysRevB.83.134114.

Delgado Mena E, Israelian G, Gonzalez Hernandez JI, et al. (2010) Chemical clues on the formation of planetary systems: C/O versus Mg/Si for HARPS GTO sample. *Astrophysical Journal* 725(2): 2349–2358. http://dx.doi.org/10.1088/0004-637X/725/2/2349.

Demory B-O, Gillon M, Seager S, Benneke B, Deming D, and Jackson B (2012) Detection of thermal emission from a super Earth. *Astrophysical Journal Letters* 751(2): L28. http://dx.doi.org/10.1088/2041-8205/751/2/L28.

Demory B-O, et al. (2011) Detection of a transit of the super-Earth 55 Cancri e with warm Spitzer. *Astronomy and Astrophysics* 533: A114. http://dx.doi.org/10.1051/0004-6361/201117178.

Dewaele A, Loubeyre P, Occelli F, Mezouar M, Dorogokupets PI, and Torrent M (2006) Quasihydrostatic equation of state of iron above 2 Mbar. *Physical Review Letters* 97(21): 215504. http://dx.doi.org/10.1103/PhysRevLett.97.215504.

Dobson DP, Hunt SA, Lindsay-Scott A, and Wood IG (2011) Towards better analogues for $MgSiO_3$ post-perovskite: $NaCoF_3$ and $NaNiF_3$, two new recoverable fluoride post-perovskites. *Physics of the Earth and Planetary Interiors* 189(3–4): 171–175. http://dx.doi.org/10.1016/j.pepi.2011.08.010.

Dorfman SM, Prakapenka VB, Meng Y, and Duffy TS (2012) Intercomparison of pressure standards (Au, Pt, Mo, MgO, NaCl and Ne) to 2.5 Mbar. *Journal of Geophysical Research: Solid Earth* 117: B082210. http://dx.doi.org/10.1029/2012JB009292.

Drake MJ and Righter K (2002) Determining the composition of the Earth. *Nature* 416(6876): 39–44. http://dx.doi.org/10.1038/416039a.

Dubrovinsky L, Dubrovinskaia N, Prakapenka VB, and Abakumov AM (2012) Implementation of micro-ball nanodiamond anvils for high-pressure studies above 6 Mbar. *Nature Communications* 3: 1163. http://dx.doi.org/10.1038/ncomms2160.

Dubrovinsky LS, Saxena SK, Tutti F, Rekhi S, and LeBehan T (2000) In situ x-ray study of thermal expansion and phase transition of iron at multimegabar pressure. *Physical Review Letters* 84(8): 1720–1723. http://dx.doi.org/10.1103/PhysRevLett.84.1720.

Dubrovinsky L, et al. (2007) Body-centered cubic iron-nickel alloy in Earth's core. *Science* 316(5833): 1880–1883. http://dx.doi.org/10.1126/science.1142105.

Duffy TS (2005) Synchrotron facilities and the study of the Earth's deep interior. *Reports on Progress in Physics* 68(8): 1811–1859. http://dx.doi.org/10.1088/0034-4885/68/8/R03.

Duffy T (2008) Some recent advances in understanding the mineralogy of Earth's deep mantle. *Philosophical Transactions of the Royal Society A: Mathematical, Physical and Engineering Sciences* 366(1883): 4273–4293. http://dx.doi.org/10.1098/rsta.2008.0172.

Duffy TS, Hemley RJ, and Mao H-K (1995) Equation of state and shear strength at multimegabar pressures: Magnesium oxide to 227 GPa. *Physical Review Letters* 74(8): 1371–1374.

Duffy TS and Wang YB (1998) Pressure–volume–temperature equations of state. In: Hemley RJ (ed.) *Ultrahigh-Pressure Mineralogy*, vol. 37, pp. 425–457. Washington, DC: Mineralogical Society of America.

Dziewonski AM and Anderson DL (1981) Preliminary reference Earth model. *Physics of the Earth and Planetary Interiors* 25(4): 297–356. http://dx.doi.org/10.1016/0031-9201(81)90046-7.

Eggert JH, Hicks DG, Celliers PM, et al. (2009) Melting temperature of diamond at ultrahigh pressure. *Nature Physics* 6(1): 40–43. http://dx.doi.org/10.1038/nphys1438.

Elkins-Tanton LT and Seager S (2008) Coreless terrestrial exoplanets. *Astrophysical Journal* 688(1): 628–635. http://dx.doi.org/10.1086/592316.

Endl M, Robertson P, Cochran WD, et al. (2012) Revisiting rho(1) Cancri e: A new mass determination of the transiting super-earth. *Astrophysical Journal* 759(1). http://dx.doi.org/10.1088/0004-637X/759/1/19.

Fat'yanov OV, Asimow PD, and Ahrens TJ (2009) Shock temperatures of preheated MgO. In: Elert M, Furnish MD, Anderson WW, Proud WG, and Butler WT (eds.) *Shock Compression of Condensed Matter 2009*, vol. 1195, pp. 855–858. Nashville, TN: AIP.

Fei YW and Mao H-K (1994) In-situ determination of the NiAs phase of FeO at high pressure and temperature. *Science* 266(5191): 1678–1680. http://dx.doi.org/10.1126/science.266.5191.1678.

Fischer RA and Campbell AJ (2010) High-pressure melting of wustite. *American Mineralogist* 95(10): 1473–1477. http://dx.doi.org/10.2138/am.2010.3463.

Fischer RA, Campbell AJ, Lord OT, Shofner GA, Dera P, and Prakapenka VB (2011) Phase transition and metallization of FeO at high pressures and temperatures. *Geophysical Research Letters* 38(24): L24301. http://dx.doi.org/10.1029/2011GL049800.

Fischer DA and Valenti J (2005) The planet-metallicity correlation. *Astrophysical Journal* 622(2): 1102–1117. http://dx.doi.org/10.1086/428383.

Fortney JJ (2012) On the carbon-to-oxygen ratio measurement in nearby sun-like stars: Implications for planet formation and the determination of stellar abundances. *Astrophysical Journal Letters* 747: L27. http://dx.doi.org/10.1088/2041-8205/747/2/L27.

Fortney JJ, Glenzer SH, Koenig M, Militzer B, Saumon D, and Valencia D (2009) Frontiers of the physics of dense plasmas and planetary interiors: Experiments, theory, and applications. *Physics of Plasmas* 16(4): 041003. http://dx.doi.org/10.1063/1.3101818.

Fortney JJ, Marley MS, and Barnes JW (2007) Planetary radii across five orders of magnitude in mass and stellar insolation: Application to transits. *Astrophysical Journal* 659(2): 1661–1672. http://dx.doi.org/10.1086/512120.

Fressin F, Torres G, Charbonneau D, et al. (2013) The false positive rate of Kepler and the occurrence of planets. *ArXiv e-prints* 1301: 842.

Funamori N and Jeanloz R (1997) High-pressure transformation of Al_2O_3. *Science* 278(5340): 1109–1111. http://dx.doi.org/10.1126/science.278.5340.1109.

Gaidos E, Conrad CP, Manga M, and Hernlund J (2010) Thermodynamic limits on magnetodynamos in rocky exoplanets. *Astrophysical Journal* 718(2): 596–609. http://dx.doi.org/10.1088/0004-637X/718/2/596.

Gaudi BS, et al. (2008) Discovery of a Jupiter/Saturn analog with gravitational microlensing. *Science* 319(5865): 927–930. http://dx.doi.org/10.1126/science.1151947.

Gelman SE, Elkins-Tanton LT, and Seager S (2011) Effects of stellar flux on tidally locked terrestrial planets: Degree-1 mantle convection and local magma ponds. *Astrophysical Journal* 735(2): 72. http://dx.doi.org/10.1088/0004-637X/735/2/72.

Gillan MJ, Alfe D, Brodholt J, Vocadlo L, and Price GD (2006) First-principles modelling of Earth and planetary materials at high pressures and temperatures. *Reports on Progress in Physics* 69(8): 2365–2441. http://dx.doi.org/10.1088/0034-4885/69/8/R03.

Gillon M, et al. (2012) Improved precision on the radius of the nearby super-Earth 55Cnc e. *Astronomy and Astrophysics* 539: A28. http://dx.doi.org/10.1051/0004-6361/201118309.

Glass CW, Oganov AR, and Hansen N (2006) USPEX – Evolutionary crystal structure prediction. *Computer Physics Communications* 175(11–12): 713–720. http://dx.doi.org/10.1016/j.cpc.2006.07.020.

Gong Y-X and Zhou J-L (2012) The silicate and carbon-rich models of CoRoT-7b, Kepler-9d and Kepler-10b. *Research in Astronomy and Astrophysics* 12(6): 678. http://dx.doi.org/10.1088/1674-4527/12/6/008.

Gramsch SA, Cohen RE, and Savrasov SY (2003) Structure, metal-insulator transitions, and magnetic properties of FeO at high pressures. *American Mineralogist* 88(2–3): 257–261.

Grasset O, Schneider J, and Sotin C (2009) A study of the accuracy of mass-radius relationships for silicate-rich and ice-rich planets up to 100 Earth masses. *Astrophysical Journal* 693(1): 722–733. http://dx.doi.org/10.1088/0004-637X/693/1/722.

Grocholski B, Shim S-H, and Prakapenka VB (2010) Stability of the $MgSiO_3$ analog $NaMgF_3$ and its implication for mantle structure in super-Earths. *Geophysical Research Letters* 37: L14204. http://dx.doi.org/10.1029/2010GL043645.

Grumbach MP and Martin RM (1996) Phase diagram of carbon at high pressures and temperatures. *Physical Review B* 54(22): 15730–15741. http://dx.doi.org/10.1103/PhysRevB.54.15730.

Hatzes AP, et al. (2011) The mass of CoRoT-7b. *Astrophysical Journal* 743(1): 75. http://dx.doi.org/10.1088/0004-637X/743/1/75.

Henning WG, O'Connell RJ, and Sasselov DD (2009) Tidally heated terrestrial exoplanets: Viscoelastic response models. *Astrophysical Journal* 707(2): 1000–1015. http://dx.doi.org/10.1088/0004-637X/707/2/1000.

Hermann A, Ashcroft NW, and Hoffmann R (2012) High pressure ices. *Proceedings of the National Academy of Sciences of the United States of America* 109(3): 745–750. http://dx.doi.org/10.1073/pnas.1118694109.

Hicks DG, Boehly TR, Celliers PM, et al. (2008) High-precision measurements of the diamond Hugoniot in and above the melt region. *Physical Review B* 78(17): 174102. http://dx.doi.org/10.1103/PhysRevB.78.174102.

Hicks DG, Boehly TR, Eggert JH, Miller JE, Celliers PM, and Collins GW (2006) Dissociation of liquid silica at high pressures and temperatures. *Physical Review Letters* 97(2): 025502. http://dx.doi.org/10.1103/PhysRevLett.97.025502.

Howard AW (2013) Observed properties of extrasolar planets. *Science* 340(6132): 572–576. http://dx.doi.org/10.1126/science.1233545.

Howard AW, et al. (2012) Planet occurrence within 0.25 AU of solar-type stars from Kepler. *Astrophysical Journal Supplement Series* 201(2): 15–39. http://dx.doi.org/10.1088/0067-0049/201/2/15.

Hubbard W, Nellis W, Mitchell A, Holmes N, Limaye S, and Mccandless P (1991) Interior structure of Neptune: Comparison with Uranus. *Science* 253(5020): 648–651. http://dx.doi.org/10.1126/science.253.5020.648.

Hunt SA, Davies DR, Walker AM, et al. (2012) On the increase in thermal diffusivity caused by the perovskite to post-perovskite phase transition and its implications for mantle dynamics. *Earth and Planetary Science Letters* 319: 96–103. http://dx.doi.org/10.1016/j.epsl.2011.12.009.

Ishikawa T, Tsuchiya T, and Tsuchiya J (2011) Stacking-disordered phase of iron in the Earth's inner core from first principles. *Physical Review B* 83(21): 212101. http://dx.doi.org/10.1103/PhysRevB.83.212101.

Jackson I and Rigden SM (1996) Analysis of P–V–T data: Constraints on the thermoelastic properties of high-pressure minerals. *Physics of the Earth and Planetary Interiors* 96(2–3): 85–112. http://dx.doi.org/10.1016/0031-9201(96)03143-3.

Jeanloz R, Ahrens TJ, Mao H-K, and Bell PM (1979) B1-B2 transition in calcium oxide from shock wave and diamond cell experiments. *Science* 206(4420): 829–830. http://dx.doi.org/10.1126/science.206.4420.829.

Ji M, Umemoto K, Wang C-Z, Ho K-M, and Wentzcovitch RM (2011) Ultrahigh-pressure phases of H_2O ice predicted using an adaptive genetic algorithm. *Physical Review B* 84(22): 220105. http://dx.doi.org/10.1103/PhysRevB.84.220105.

Johnson JD (1999) A bound and estimate for the maximum compression of single shocks. *Physical Review E* 59(3): 3727–3728. http://dx.doi.org/10.1103/PhysRevE.59.3727.

Kalas P, Graham JR, Chiang E, et al. (2008) Optical images of an exosolar planet 25 light-years from Earth. *Science* 322(5906): 1345–1348. http://dx.doi.org/10.1126/science.1166609.

Karato S (1989) Plasticity crystal-structure systematics in dense oxides and its implications for the creep strength of the Earth's deep interior: A preliminary result. *Physics of the Earth and Planetary Interiors* 55(3–4): 234–240. http://dx.doi.org/10.1016/0031-9201(89)90071-X.

Karato S (2008) *Deformation of Earth Materials: Introduction to the Rheology of the Solid Earth*. Cambridge: Cambridge University Press.

Karato S (2010) The influence of anisotropic diffusion on the high-temperature creep of a polycrystalline aggregate. *Physics of the Earth and Planetary Interiors* 183(3–4): 468–472. http://dx.doi.org/10.1016/j.pepi.2010.09.001.

Karato S (2011) Rheological structure of the mantle of a super-Earth: Some insights from mineral physics. *Icarus* 212(1): 14–23. http://dx.doi.org/10.1016/j.icarus.2010.12.005.

Kargel J and Lewis J (1993) The composition and early evolution of Earth. *Icarus* 105(1): 1–25. http://dx.doi.org/10.1006/icar.1993.1108.

Karki B, Stixrude L, Clark S, Warren M, Ackland G, and Crain J (1997a) Structure and elasticity of MgO at high pressure. *American Mineralogist* 82(1–2): 51–60.

Karki BB, Stixrude L, and Crain J (1997b) Ab initio elasticity of three high-pressure polymorphs of silica. *Geophysical Research Letters* 24(24): 3269–3272. http://dx.doi.org/10.1029/97GL53196.

Kingma KJ, Cohen RE, Hemley RJ, and Mao HK (1995) Transformation of stishovite to a denser phase at lower mantle pressures. *Nature* 374(6519): 243–245.

Knudson MD and Desjarlais M (2009) Shock compression of quartz to 1.6 TPa: Redefining a pressure standard. *Physical Review Letters* 103(22): 225501. http://dx.doi.org/10.1103/PhysRevLett.103.225501.

Knudson MD, Desjarlais MP, and Dolan DH (2008) Shock-wave exploration of the high-pressure phases of carbon. *Science* 322(5909): 1822–1825. http://dx.doi.org/10.1126/science.1165278.

Korenaga J (2010) On the likelihood of plate tectonics on super-Earths: Does size matter? *Astrophysical Journal Letters* 725(1): L43–L46. http://dx.doi.org/10.1088/2041-8205/725/1/L43.

Kraus RG, et al. (2012) Shock vaporization of silica and the thermodynamics of planetary impact events. *Journal of Geophysical Research: Planets* 117: E09009. http://dx.doi.org/10.1029/2012JE004082.

Kubo A, Kiefer B, Shen G, Prakapenka V, Cava R, and Duffy T (2006) Stability and equation of state of the post-perovskite phase in $MgGeO_3$ to 2 Mbar. *Geophysical Research Letters* 33(12): L12812. http://dx.doi.org/10.1029/2006GL025686.

Kuchner MJ and Seager S (2005) Extrasolar carbon planets. arXiv:astro-ph/0504214.

Kuwayama Y, Hirose K, Sata N, and Ohishi Y (2005) The pyrite-type high-pressure form of silica. *Science* 309(5736): 923–925. http://dx.doi.org/10.1126/science.1114879.

Kuwayama Y, Hirose K, Sata N, and Ohishi Y (2008) Phase relations of iron and iron-nickel alloys up to 300 GPa: Implications for composition and structure of the Earth's inner core. *Earth and Planetary Science Letters* 273(3–4): 379–385. http://dx.doi.org/10.1016/j.epsl.2008.07.001.

Labrosse S, Hernlund JW, and Coltice N (2007) A crystallizing dense magma ocean at the base of the Earth's mantle. *Nature* 450(7171): 866–869. http://dx.doi.org/10.1038/nature06355.

Lecavelier des Etangs A, Vidal-Madjar A, McConnel JC, and Hebrard G (2004) Atmospheric escape from hot Jupiters. *Astronomy and Astrophysics* 418(1): L1–L4. http://dx.doi.org/10.1051/0004-6361:20040106.

Léger A, et al. (2004) A new family of planets? 'Ocean-Planets'. *Icarus* 169(2): 499–504. http://dx.doi.org/10.1016/j.icarus.2004.01.001.

Léger A, et al. (2009) Transiting exoplanets from the CoRoT space mission VIII. CoRoT-7b: The first super-Earth with measured radius. *Astronomy and Astrophysics* 506(1): 287–302. http://dx.doi.org/10.1051/0004-6361/200911933.

Léger A, et al. (2011) The extreme physical properties of the CoRoT-7b super-Earth. *Icarus* 213(1): 1–11. http://dx.doi.org/10.1016/j.icarus.2011.02.004.

Leitzinger M, et al. (2011) Could CoRoT-7b and Kepler-10b be remnants of evaporated gas or ice giants? *Planetary and Space Science* 59(13): 1472–1481. http://dx.doi.org/10.1016/j.pss.2011.06.003.

Lin J-F, Speziale S, Mao Z, and Marquardt H (2013) Effects of the electronic spin transitions of iron in lower mantle minerals: Implications for deep mantle geophysics and geochemistry. *Reviews of Geophysics* 51: 244–275.

Lopez ED, Fortney JJ, and Miller N (2012) How thermal evolution and mass-loss sculpt populations of super-Earths and sub-Neptunes: Application to the Kepler-11 system and beyond. *Astrophysical Journal* 761(1): 59. http://dx.doi.org/10.1088/0004-637X/761/1/59.

Lorenz KT, Edwards MJ, Glendinning SG, et al. (2005) Accessing ultrahigh-pressure, quasi-isentropic states of matter. *Physics of Plasmas* 12(5): 056309. http://dx.doi.org/10.1063/1.1873812.

Lundin S, Catalli K, Santillán J, et al. (2008) Effect of Fe on the equation of state of mantle silicate perovskite over 1 Mbar. *Physics of the Earth and Planetary Interiors* 168(1–2): 97–102. http://dx.doi.org/10.1016/j.pepi.2008.05.002.

Luo S-N, Akins JA, Ahrens TJ, and Asimow PD (2004) Shock-compressed $MgSiO_3$ glass, enstatite, olivine, and quartz: Optical emission, temperatures, and melting. *Journal of Geophysical Research* 109: B05205. http://dx.doi.org/10.1029/2003JB002860.

Luo W, Johansson B, Eriksson O, et al. (2010) Dynamical stability of body center cubic iron at the Earth's core conditions. *Proceedings of the National Academy of Sciences* 107(22): 9962–9964. http://dx.doi.org/10.1073/pnas.1004076107.

Lyzenga GA, Ahrens TJ, and Mitchell AC (1983) Shock temperatures of SiO_2 and their geophysical implications. *Journal of Geophysical Research* 88(NB3): 2431–2444.

Ma YZ, Somayazulu M, Shen GY, Mao H-K, Shu JF, and Hemley RJ (2004) In situ x-ray diffraction studies of iron to Earth-core conditions. *Physics of the Earth and Planetary Interiors* 143: 455–467. http://dx.doi.org/10.1016/j.pepi.2003.06.005.

Madhusudhan N, Lee KKM, and Mousis O (2012) A possible carbon-rich interior in super-earth 55 Cancri e. *Astrophysical Journal Letters* 759(2): L40. http://dx.doi.org/10.1088/2041-8205/759/2/L40.

Madhusudhan N, et al. (2011) A high C/O ratio and weak thermal inversion in the atmosphere of exoplanet WASP-12b. *Nature* 469(7328): 64–67. http://dx.doi.org/10.1038/nature09602.

Marcy GW and Butler RP (1996) A planetary companion to 70 Virginis. *Astrophysical Journal* 464(2): L147–L151. http://dx.doi.org/10.1086/310096.

Martin CD, Crichton WA, Liu HZ, Prakapenka V, Chen JH, and Parise JB (2006) Phase transitions and compressibility of $NaMgF_3$ (Neighborite) in perovskite- and post-perovskite-related structures. *Geophysical Research Letters* 33(11): L11305. http://dx.doi.org/10.1029/2006GL026150.

Martinez-Canales M, Pickard CJ, and Needs RJ (2012) Thermodynamically stable phases of carbon at multiterapascal pressures. *Physical Review Letters* 108(4): 045704. http://dx.doi.org/10.1103/PhysRevLett.108.045704.

Marton F and Cohen R (1994) Prediction of a high-pressure phase-transition in Al_2O_3. *American Mineralogist* 79(7–8): 789–792.

Matzen MK, et al. (2005) Pulsed-power-driven high energy density physics and inertial confinement fusion research. *Physics of Plasmas* 12(5). http://dx.doi.org/10.1063/1.1891746.

Mayor M and Queloz D (1995) A Jupiter-mass companion to a solar-type star. *Nature* 378(6555): 355–359. http://dx.doi.org/10.1038/378355a0.

McDonough WF and Sun S-S (1995) The composition of the Earth. *Chemical Geology* 120(3–4): 223–253. http://dx.doi.org/10.1016/0009-2541(94)00140-4.

McWilliams RS, Spaulding DK, Eggert JH, et al. (2012) Phase transformations and metallization of magnesium oxide at high pressure and temperature. *Science* 338(6112): 1330–1333. http://dx.doi.org/10.1126/science.1229450.

Mehl MJ, Cohen RE, and Krakauer H (1988) Linearized augmented plane-wave electronic-structure calculations for MgO and CaO. *Journal of Geophysical Research* 93(B7): 8009–8022. http://dx.doi.org/10.1029/JB093iB07p08009.

Melosh HJ (2007) A hydrocode equation of state for SiO_2. *Meteoritics and Planetary Science* 42(12): 2079–2098. http://dx.doi.org/10.1111/j.1945-5100.2007.tb01009.x.

Mikhaylushkin AS, Abrikosov IA, Belonoshko AB, Johansson B, and Simak SI (2009) Instability of the body-centered tetragonal phase of iron under extreme conditions. *Physical Review B* 79(13): 132106. http://dx.doi.org/10.1103/PhysRevB.79.132106.

Militzer B and Hubbard WB (2009) Comparison of Jupiter interior models derived from first-principles simulations. *Astrophysics and Space Science* 322(1–4): 129–133. http://dx.doi.org/10.1007/s10509-008-9958-5.

Militzer B and Wilson HF (2010) New phases of water ice predicted at megabar pressures. *Physical Review Letters* 105(19): 195701. http://dx.doi.org/10.1103/PhysRevLett.105.195701.

Miller-Ricci E and Fortney JJ (2010) The nature of the atmosphere of the transiting super-earth GJ1214b. *Astrophysical Journal Letters* 716(1): L74–L79. http://dx.doi.org/10.1088/2041-8205/716/1/L74.

Modak P, Verma AK, Rao RS, Godwal BK, Stixrude L, and Jeanloz R (2007) Stability of the hcp phase and temperature variation of the axial ratio of iron near Earth-core conditions. *Journal of Physics: Condensed Matter* 19(1): 016208. http://dx.doi.org/10.1088/0953-8984/19/1/016208.

Moore WB (2003) Tidal heating and convection in Io. *Journal of Geophysical Research: Planets* 108(E8): 5096. http://dx.doi.org/10.1029/2002JE001943.

Morard G, Bouchet J, Valencia D, Mazevet S, and Guyot F (2011) The melting curve of iron at extreme pressures: Implications for planetary cores. *High Energy Density Physics* 7(3): 141–144. http://dx.doi.org/10.1016/j.hedp.2011.02.001.

Morley C, Fortney JJ, Kempton E, Visscher CW, and Marley MS (2013) The effect of clouds and hazes on the transmission spectrum of GJ 1214b. In: *American Astronomical Society Meeting Abstracts*, vol. 221.

Mosenfelder JL, Asimow PD, Frost DJ, Rubie DC, and Ahrens TJ (2009) The $MgSiO_3$ system at high pressure: Thermodynamic properties of perovskite, postperovskite, and melt from global inversion of shock and static compression data. *Journal of Geophysical Research: Solid Earth* 114: B01203. http://dx.doi.org/10.1029/2008JB005900.

Moses E (2011) The National Ignition Facility: An experimental platform for studying behavior of matter under extreme conditions. *Astrophysics and Space Science* 336(1): 3–7. http://dx.doi.org/10.1007/s10509-010-0536-2.

Murakami M, Hirose K, Ono S, and Ohishi Y (2003) Stability of $CaCl_2$-type and α-PbO_2-type SiO_2 at high pressure and temperature determined by in-situ x-ray measurements. *Geophysical Research Letters* 30(5): 1207.

Nagao H, et al. (2006) Hugoniot measurement of diamond under laser shock compression up to 2 TPa. *Physics of Plasmas* 13(5). http://dx.doi.org/10.1063/1.2205194.

Nellis WJ (2007) Adiabat-reduced isotherms at 100 GPa pressures. *High Pressure Research* 27(4): 393–407. http://dx.doi.org/10.1080/08957950701659734.

Nellis WJ (2010) Al_2O_3 as a metallic glass at 300 GPa. *Physical Review B* 82(9): 092101. http://dx.doi.org/10.1103/PhysRevB.82.092101.

Nellis WJ (2012) Possible magnetic fields of super Earths generated by convecting, conducting oxides. *AIP Conference Proceedings* 1426(1): 863–866. http://dx.doi.org/10.1063/1.3686414.

Nguyen JH and Holmes NC (2004) Melting of iron at the physical conditions of the Earth's core. *Nature* 427(6972): 339–342. http://dx.doi.org/10.1038/nature02248.

Nishio-Hamane D, Zhang M, Yagi T, and Ma Y (2012) High-pressure and high-temperature phase transitions in $FeTiO_3$ and a new dense $FeTi_3O_7$ structure. *American Mineralogist* 97(4): 568–572. http://dx.doi.org/10.2138/am.2012.3973.

Nissen PE (2013) *The Carbon-to-Oxygen Ratio in Stars with Planets*, arXiv e-print. (online) Available from http://arxiv.org/abs/1303.1726 (accessed 26 August 2013).

Occelli F, Loubeyre P, and Letoullec R (2003) Properties of diamond under hydrostatic pressures up to 140 GPa. *Nature Materials* 2(3): 151–154. http://dx.doi.org/10.1038/nmat831.

Oganov A, Gillan M, and Price G (2003) Ab initio lattice dynamics and structural stability of MgO. *Journal of Chemical Physics* 118(22): 10174–10182. http://dx.doi.org/10.1063/1.1570394.

Oganov A, Gillan M, and Price G (2005) Structural stability of silica at high pressures and temperatures. *Physical Review B* 71(6): 064104. http://dx.doi.org/10.1103/PhysRevB.71.064104.

Oganov AR, Hemley RJ, Hazen RM, and Jones AP (2013) Structure, bonding, and mineralogy of carbon at extreme conditions. *Reviews in Mineralogy and Geochemistry* 75: 47–77.

Oganov AR and Ono S (2005) The high-pressure phase of alumina and implications for Earth's D″ layer. *Proceedings of the National Academy of Sciences of the United States of America* 102(31): 10828–10831. http://dx.doi.org/10.1073/pnas.0501800102.

Ohta K, Cohen RE, Hirose K, Haule K, Shimizu K, and Ohishi Y (2012a) Experimental and theoretical evidence for pressure-induced metallization in FeO with rocksalt-type structure. *Physical Review Letters* 108(2): 026403. http://dx.doi.org/10.1103/PhysRevLett.108.026403.

Ohta K, Yagi T, Taketoshi N, et al. (2012b) Lattice thermal conductivity of $MgSiO_3$ perovskite and post-perovskite at the core-mantle boundary. *Earth and Planetary Science Letters* 349: 109–115. http://dx.doi.org/10.1016/j.epsl.2012.06.043.

Okada T, Yagi T, and Nishio-Hamane D (2011) High-pressure phase behavior of $MnTiO_3$: Decomposition of perovskite into MnO and $MnTi_2O_5$. *Physics and Chemistry of Minerals* 38(4): 251–258. http://dx.doi.org/10.1007/s00269-010-0400-5.

Ozawa H, Takahashi F, Hirose K, Ohishi Y, and Hirao N (2011) Phase transition of FeO and stratification in Earth's outer core. *Science* 334(6057): 792–794. http://dx.doi.org/10.1126/science.1208265.

Petigura EA and Marcy GW (2011) Carbon and oxygen in nearby stars: Keys to protoplanetary disk chemistry. *Astrophysical Journal* 735(1): 41. http://dx.doi.org/10.1088/0004-637X/735/1/41.

Pickard CJ and Needs RJ (2009) Stable phases of iron at terapascal pressures. *Journal of Physics: Condensed Matter* 21(45): 452205. http://dx.doi.org/10.1088/0953-8984/21/45/452205.

Pickard CJ and Needs RJ (2011) Ab initio random structure searching. *Journal of Physics: Condensed Matter* 23(5): 053201. http://dx.doi.org/10.1088/0953-8984/23/5/053201.

Poirier J-P (1985) *Creep of Crystals: High-Temperature Deformation Processes in Metals, Ceramics and Minerals*. Cambridge: Cambridge University Press.

Poirier J-P (2000) *Introduction to the Physics of the Earth's Interior*, 2nd edn. Cambridge: Cambridge University Press.

Rogers L and Seager S (2010) A framework for quantifying the degeneracies of exoplanet interior compositions. *Astrophysical Journal* 712(2): 974–991. http://dx.doi.org/10.1088/0004-637X/712/2/974.

Ross M (1981) The ice layer in Uranus and Neptune: Diamonds in the sky? *Nature* 292(5822): 435–436. http://dx.doi.org/10.1038/292435a0.

Ross I, White M, Boon J, et al. (1981) Vulcan: A versatile high-power glass-laser for multiuser experiments. *IEEE Journal of Quantum Electronics* 17(9): 1653–1661. http://dx.doi.org/10.1109/JQE.1981.1071308.

Rygg JR, et al. (2012) Powder diffraction from solids in the terapascal regime. *Review of Scientific Instruments* 83(11): 113904. http://dx.doi.org/10.1063/1.4766464.

Salpeter E and Zapolsky H (1967) Theoretical high-pressure equations of state including correlation energy. *Physics Review* 158(3): 876–886. http://dx.doi.org/10.1103/PhysRev.158.876.

Schaefer L, Lodders K, and Fegley B (2012) Vaporization of the earth: Application to exoplanet atmospheres. *Astrophysical Journal* 755(1): 41. http://dx.doi.org/10.1088/0004-637X/755/1/41.

Seager S (2013) Exoplanet habitability. *Science* 340(6132): 577–581. http://dx.doi.org/10.1126/science.1232226.

Seager S and Deming D (2010) Exoplanet atmospheres. In: Blandford R, Faber SM, VanDishoeck E, and Kormendy J (eds.) *Annual Review of Astronomy and Astrophysics*, vol. 48, pp. 631–672. Palo Alto, CA: Annual Reviews.

Seager S, Kuchner M, Hier-Majumder CA, and Militzer B (2007) Mass-radius relationships for solid exoplanets. *Astrophysical Journal* 669(2): 1279–1297. http://dx.doi.org/10.1086/521346.

Sekine T and Kobayashi T (1997) Shock compression of 6H polytype SiC to 160 GPa. *Physical Review B* 55(13): 8034–8037. http://dx.doi.org/10.1103/PhysRevB.55.8034.

Shen GY, Mao H-K, Hemley RJ, Duffy TS, and Rivers ML (1998) Melting and crystal structure of iron at high pressures and temperatures. *Geophysical Research Letters* 25(3): 373–376.

Sokolov PS, Mukhanov VA, Chauveau T, and Solozhenko VL (2012) On melting of silicon carbide under pressure. *Journal of Superhard Materials* 34(5): 339–341. http://dx.doi.org/10.3103/S1063457612050097.

Somayazulu M, Shu J, Zha C, et al. (2008) In situ high-pressure x-ray diffraction study of H_2O ice VII. *Journal of Chemical Physics* 128(6): 064510. http://dx.doi.org/10.1063/1.2813890.

Sotin C, Grasset O, and Mocquet A (2007) Mass–radius curve for extrasolar Earth-like planets and ocean planets. *Icarus* 191(1): 337–351. http://dx.doi.org/10.1016/j.icarus.2007.04.006.

Sotin C, Jackson JM, and Seager S (2010) Terrestrial planet interiors. In: Seager S (ed.) *Exoplanets*, pp. 375–395. Tucson, AZ: University of Arizona.

Spaulding DK, McWilliams RS, Jeanloz R, et al. (2012) Evidence for a phase transition in silicate melt at extreme pressure and temperature conditions. *Physical Review Letters* 108(6): 065701. http://dx.doi.org/10.1103/PhysRevLett.108.065701.

Stacey FD (2000) The K-primed approach to high-pressure equations of state. *Geophysical Journal International* 143(3): 621–628. http://dx.doi.org/10.1046/j.1365-246X.2000.00253.x.

Stacey FD and Davis PM (2004) High pressure equations of state with applications to the lower mantle and core. *Physics of the Earth and Planetary Interiors* 142(3–4): 137–184. http://dx.doi.org/10.1016/j.pepi.2004.02.003.

Stamenkovic V, Breuer D, and Spohn T (2011) Thermal and transport properties of mantle rock at high pressure: Applications to super-Earths. *Icarus* 216(2): 572–596. http://dx.doi.org/10.1016/j.icarus.2011.09.030.

Stamenkovic V, Noack L, Breuer D, and Spohn T (2012) The influence of pressure-dependent viscosity on the thermal evolution of super-Earths. *Astrophysical Journal* 748(1): 41. http://dx.doi.org/10.1088/0004-637X/748/1/41.

Stixrude L (2012) Structure of iron to 1 Gbar and 40 000 K. *Physical Review Letters* 108(5): 055505. http://dx.doi.org/10.1103/PhysRevLett.108.055505.

Strachan A, Cagin T, and Goddard W (1999) Phase diagram of MgO from density-functional theory and molecular-dynamics simulations. *Physical Review B* 60(22): 15084–15093.

Svendsen B and Ahrens T (1987) Shock-induced temperatures of MgO. *Geophysical Journal of the Royal Astronomical Society* 91(3): 667–691.

Swift DC, Eggert JH, Hicks DG, et al. (2012) Mass-radius relationships for exoplanets. *Astrophysical Journal* 744(1): 59. http://dx.doi.org/10.1088/0004-637X/744/1/59.

Tachinami C, Senshu H, and Ida S (2011) Thermal evolution and lifetime of intrinsic magnetic fields of super-earths in habitable zones. *Astrophysical Journal* 726(2): 70. http://dx.doi.org/10.1088/0004-637X/726/2/70.

Tackley PJ, Ammann M, Brodholt JP, Dobson DP, and Valencia D (2013) Mantle dynamics in super-Earths: Post-perovskite rheology and self-regulation of viscosity. *Icarus* 225: 50–61.

Tackley P, Stevenson D, Glatzmaier G, and Schubert G (1993) Effects of an endothermic phase-transition at 670 km depth in a spherical model of convection in the Earth's mantle. *Nature* 361(6414): 699–704. http://dx.doi.org/10.1038/361699a0.

Tangney P and Scandolo S (2009) Melting slope of MgO from molecular dynamics and density functional theory. *Journal of Chemical Physics* 131(12): 124510. http://dx.doi.org/10.1063/1.3238548.

Tateno S, Hirose K, Ohishi Y, and Tatsumi Y (2010) The structure of iron in Earth's inner core. *Science* 330(6002): 359–361. http://dx.doi.org/10.1126/science.1194662.

Thompson SL (1990) ANEOS: Analytic equations of state for shock physics codes. Sandia National Laboratories Report SAND89-2951.

Thompson SL and Lauson HL (1972) Improvements in the Chart-D radiation hydrodynamics code III: Revised analytical equation of state. Sandia National Laboratory Report SC-RR-710714.

Tosi N, Yuen DA, and Cadek O (2010) Dynamical consequences in the lower mantle with the post-perovskite phase change and strongly depth-dependent thermodynamic and transport properties. *Earth and Planetary Science Letters* 298(1–2): 229–243. http://dx.doi.org/10.1016/j.epsl.2010.08.001.

Tronnes RG (2010) Structure, mineralogy and dynamics of the lowermost mantle. *Mineralogy and Petrology* 99(3–4): 243–261.

Tsuchida Y and Yagi T (1989) A new, post-stishovite high-pressure polymorph of silica. *Nature* 340(6230): 217–220. http://dx.doi.org/10.1038/340217a0.

Tsuchiya T and Tsuchiya J (2011) Prediction of a hexagonal SiO_2 phase affecting stabilities of $MgSiO_3$ and $CaSiO_3$ at multimegabar pressures. *Proceedings of the National Academy of Sciences of the United States of America* 108(4): 1252–1255. http://dx.doi.org/10.1073/pnas.1013594108.

Umemoto K and Wentzcovitch RM (2008) Prediction of an U_2S_3-type polymorph of Al_2O_3 at 3.7 Mbar. *Proceedings of the National Academy of Sciences* 105(18): 6526–6530. http://dx.doi.org/10.1073/pnas.0711925105.

Umemoto K and Wentzcovitch RM (2011) Two-stage dissociation in $MgSiO_3$ post-perovskite. *Earth and Planetary Science Letters* 311(3–4): 225–229. http://dx.doi.org/10.1016/j.epsl.2011.09.032.

Umemoto K, Wentzcovitch RM, and Allen PB (2006a) Dissociation of $MgSiO_3$ in the cores of gas giants and terrestrial exoplanets. *Science* 311(5763): 983–986. http://dx.doi.org/10.1126/science.1120865.

Umemoto K, Wentzcovitch RM, Weidner DJ, and Parise JB (2006b) $NaMgF_3$: A low-pressure analog of $MgSiO_3$. *Geophysical Research Letters* 33(15): L15304. http://dx.doi.org/10.1029/2006GL026348.

Valencia D (2013) Composition and internal dynamics of super-Earths. In: Karato S-I (ed.) *Physics and Chemistry of the Deep Earth*, pp. 271–294. Hoboken, NJ: Wiley.

Valencia D, O'Connell RJ, and Sasselov D (2006) Internal structure of massive terrestrial planets. *Icarus* 181(2): 545–554. http://dx.doi.org/10.1016/j.icarus.2005.11.021.

Valencia D, O'Connell RJ, and Sasselov DD (2009) The role of high-pressure experiments on determining super-Earth properties. *Astrophysics and Space Science* 322(1–4): 135–139. http://dx.doi.org/10.1007/s10509-009-0034-6.

Valencia D, Sasselov DD, and O'Connell RJ (2007a) Detailed models of super-Earths: How well can we infer bulk properties? *Astrophysical Journal* 665(2): 1413–1420. http://dx.doi.org/10.1086/519554.

Valencia D, Sasselov DD, and O'Connell RJ (2007b) Radius and structure models of the first super-earth planet. *Astrophysical Journal* 656(1): 545–551. http://dx.doi.org/10.1086/509800.

Van den Berg AP, Yuen DA, Beebe GL, and Christiansen MD (2010) The dynamical impact of electronic thermal conductivity on deep mantle convection of exosolar planets. *Physics of the Earth and Planetary Interiors* 178(3–4): 136–154. http://dx.doi.org/10.1016/j.pepi.2009.11.001.

Van Heck HJ and Tackley PJ (2011) Plate tectonics on super-Earths: Equally or more likely than on Earth. *Earth and Planetary Science Letters* 310(3–4): 252–261. http://dx.doi.org/10.1016/j.epsl.2011.07.029.

Verlet L (1967) Computer experiments on classical fluids I. Thermodynamical properties of Lennard–Jones molecules. *Physics Review* 159(1): 98–103. http://dx.doi.org/10.1103/PhysRev.159.98.

Vilim R, Stanley S, and Elkins-Tanton L (2013) The effect of lower mantle metallization on magnetic field generation in rocky exoplanets. *Astrophysical Journal Letters* 768(2): L30. http://dx.doi.org/10.1088/2041-8205/768/2/L30.

Vinet P, Ferrante J, Smith J, and Rose J (1986) A universal equation of state for solids. *Journal of Physics C: Solid State Physics* 19(20): L467–L473. http://dx.doi.org/10.1088/0022-3719/19/20/001.

Vinet P, Rose J, Ferrante J, and Smith J (1989) Universal features of the equation of state of solids. *Journal of Physics: Condensed Matter* 1(11): 1941–1963. http://dx.doi.org/10.1088/0953-8984/1/11/002.

Vočadlo L, Brodholt J, Alfè D, Price GD, and Gillan MJ (1999) The structure of iron under the conditions of the Earth's inner core. *Geophysical Research Letters* 26(9): 1231–1234. http://dx.doi.org/10.1029/1999GL900214.

Wagner FW, Sohl F, Hussmann H, Grott M, and Rauer H (2011) Interior structure models of solid exoplanets using material laws in the infinite pressure limit. *Icarus* 214(2): 366–376. http://dx.doi.org/10.1016/j.icarus.2011.05.027.

Wagner FW, Tosi N, Sohl F, Rauer H, and Spohn T (2012) Rocky super-Earth interiors. *Astronomy and Astrophysics* 541: A103. http://dx.doi.org/10.1051/0004-6361/201118441.

Wang J, He D, and Duffy TS (2010) Stress state of diamond and gold under nonhydrostatic compression to 360 GPa. *Journal of Applied Physics* 108(6): 063521. http://dx.doi.org/10.1063/1.3485828.

Wang X, Scandolo S, and Car R (2005) Carbon phase diagram from ab initio molecular dynamics. *Physical Review Letters* 95(18): 185701. http://dx.doi.org/10.1103/PhysRevLett.95.185701.

Wang J, Smith RF, Eggert JH, et al. (2013) Ramp compression of iron to 273 GPa. *Journal of Applied Physics* 114: 023513.

Wentzcovitch R and Stixrude L (eds.) (2010) *Theoretical and Computational Methods in Mineral Physics: Geophysical Applications, Reviews in Mineralogy and Geochemistry*. Chantilly, VA: Mineralogical Society of America.

Wentzcovitch RM, Yu YG, and Wu Z (2010) Thermodynamic properties and phase relations in mantle minerals investigated by first principles quasiharmonic theory. In: Wentzcovitch R and Stixrude L (eds.) *Theoretical and Computational Methods in Mineral Physics: Geophysical Applications*, vol. 71, pp. 59–98. Chantilly, VA: Mineralogical Society of America.

Wilson HF and Militzer B (2012) Rocky core solubility in Jupiter and giant exoplanets. *Physical Review Letters* 108(11): 111101. http://dx.doi.org/10.1103/PhysRevLett.108.111101.

Winn JN, et al. (2011) A super-Earth transiting a naked-eye star. *Astrophysical Journal* 737(1): L18. http://dx.doi.org/10.1088/2041-8205/737/1/L18.

Wolszczan A and Frail D (1992) A planetary system around the millisecond pulsar PSR1257+12. *Nature* 355(6356): 145–147. http://dx.doi.org/10.1038/355145a0.

Wright JT, et al. (2011) The exoplanet orbit database. *Publications of the Astronomical Society of the Pacific* 123(902): 412–422. http://dx.doi.org/10.1086/659427.

Wu CJ, Glosli JN, Galli G, and Ree FH (2002) Liquid-liquid phase transition in elemental carbon: A first-principles investigation. *Physical Review Letters* 89(13): 135701. http://dx.doi.org/10.1103/PhysRevLett.89.135701.

Wu X, Steinle-Neumann G, Narygina O, et al. (2009) High-pressure behavior of perovskite: $FeTiO_3$ dissociation into $(Fe_{1-\delta}, Ti_\delta)O$ and $Fe_{1+\delta}Ti_{2-\delta}O_5$. *Physical Review Letters* 103(6): 065503. http://dx.doi.org/10.1103/PhysRevLett.103.065503.

Wu S, Umemoto K, Ji M, Wang C-Z, Ho K-M, and Wentzcovitch RM (2011) Identification of post-pyrite phase transitions in SiO_2 by a genetic algorithm. *Physical Review B* 83(18): 184102. http://dx.doi.org/10.1103/PhysRevB.83.184102.

Yamanaka T, Hirose K, Mao WL, et al. (2012) Crystal structures of $(Mg_{1-x}, Fe_x)SiO_3$ postperovskite at high pressures. *Proceedings of the National Academy of Sciences of the United States of America* 109(4): 1035–1040. http://dx.doi.org/10.1073/pnas.1118076108.

Yin MT (1984) Si-III (BC-8) crystal phase of Si and C: Structural properties, phase stabilities, and phase transitions. *Physical Review B* 30(4): 1773–1776. http://dx.doi.org/10.1103/PhysRevB.30.1773.

Yin MT and Cohen ML (1983) Will diamond transform under megabar pressures? *Physical Review Letters* 50(25): 2006–2009. http://dx.doi.org/10.1103/PhysRevLett.50.2006.

Yoshida M, Onodera A, Ueno M, Takemura K, and Shimomura O (1993) Pressure-induced phase transition in SiC. *Physical Review B* 48(14): 10587–10590. http://dx.doi.org/10.1103/PhysRevB.48.10587.

Zerr A and Boehler R (1994) Constraints on the melting temperature of the lower mantle from high-pressure experiments on MgO and magnesiowustite. *Nature* 371(6497): 506–508. http://dx.doi.org/10.1038/371506a0.

Zhang L and Fei Y (2008) Melting behavior of (Mg, Fe)O solid solutions at high pressure. *Geophysical Research Letters* 35(13): L13302. http://dx.doi.org/10.1029/2008GL034585.

Zhang L, Gong Z, and Fei Y (2008) Shock-induced phase transitions in the MgO–FeO system to 200 GPa. *Journal of Physics and Chemistry of Solids* 69(9): 2344–2348. http://dx.doi.org/10.1016/j.jpcs.2008.04.006.

Zhu Q, Oganov AR, and Lyakhov AO (2013) Novel stable compounds in the Mg–O system under high pressure. *Physical Chemistry Chemical Physics* 15(20): 7696–7700. http://dx.doi.org/10.1039/C3CP50678A.